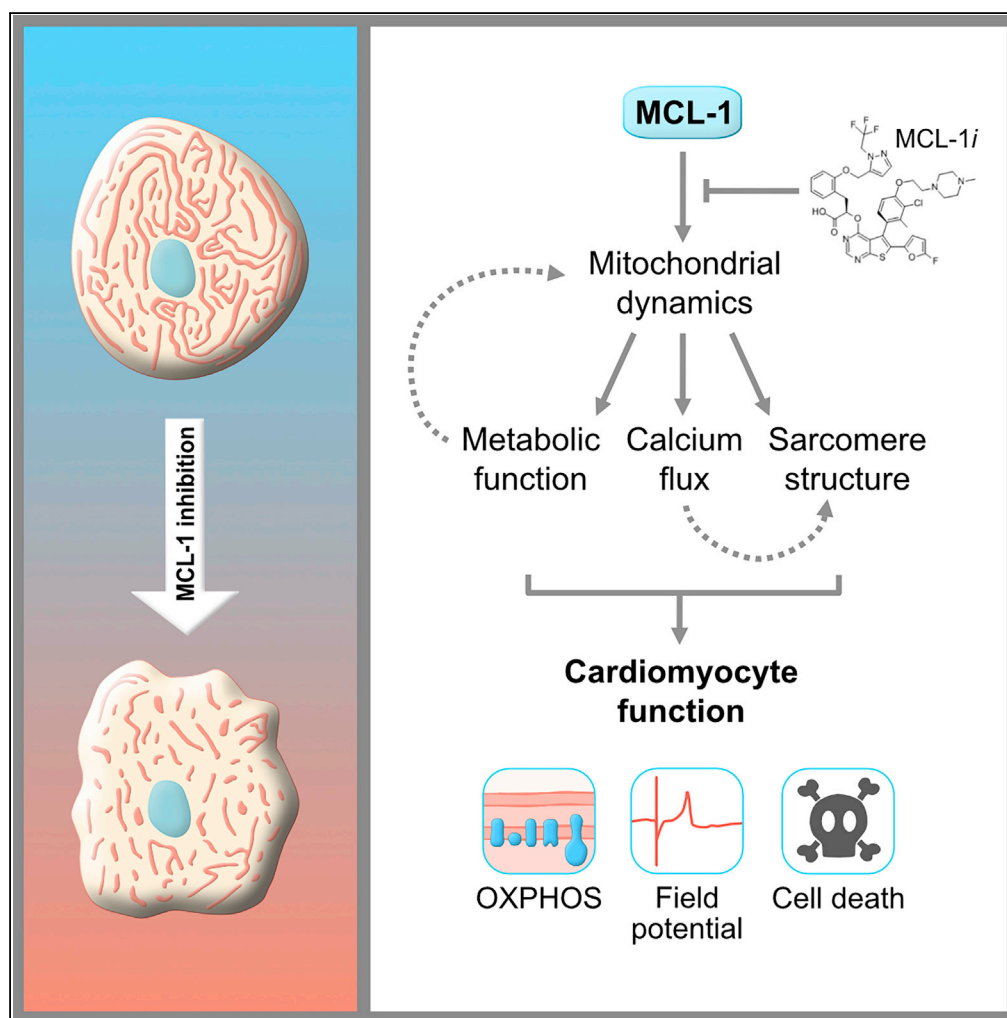


Article

MCL-1 Inhibition by Selective BH3 Mimetics Disrupts Mitochondrial Dynamics Causing Loss of Viability and Functionality of Human Cardiomyocytes



Megan L. Rasmussen, Nilay Taneja, Abigail C. Neining, ..., Bjorn C. Knollmann, Dylan T. Burnette, Vivian Gama

vivian.gama@vanderbilt.edu

HIGHLIGHTS

BH3 mimetics targeting MCL-1 disrupt the mitochondrial network of human iPSC-CMs

The BH3-mimetic-mediated effects on mitochondrial dynamics are DRP-1-dependent

Targeting MCL-1 affects the survival and function of human cardiomyocytes

Human iPSC-derived cardiomyocytes can be used to reveal toxicity of MCL-1 inhibitors

Rasmussen et al., iScience 23, 101015
 April 24, 2020 © 2020 The Author(s).
<https://doi.org/10.1016/j.isci.2020.101015>

Article

MCL-1 Inhibition by Selective BH3 Mimetics Disrupts Mitochondrial Dynamics Causing Loss of Viability and Functionality of Human Cardiomyocytes

Megan L. Rasmussen,^{1,7} Nilay Taneja,^{1,7} Abigail C. Neiningner,¹ Lili Wang,^{2,6} Gabriella L. Robertson,¹ Stellan N. Riffle,¹ Linzheng Shi,¹ Bjorn C. Knollmann,^{2,6} Dylan T. Burnette,^{1,3,5} and Vivian Gama^{1,3,4,5,8,*}

SUMMARY

MCL-1 is a well-characterized inhibitor of cell death that has also been shown to be a regulator of mitochondrial dynamics in human pluripotent stem cells. We used cardiomyocytes derived from human-induced pluripotent stem cells (hiPSC-CMs) to uncover whether MCL-1 is crucial for cardiac function and survival. Inhibition of MCL-1 by BH3 mimetics resulted in the disruption of mitochondrial morphology and dynamics as well as disorganization of the actin cytoskeleton. Interfering with MCL-1 function affects the homeostatic proximity of DRP-1 and MCL-1 at the outer mitochondrial membrane, resulting in decreased functionality of hiPSC-CMs. Cardiomyocytes display abnormal cardiac performance even after caspase inhibition, supporting a nonapoptotic activity of MCL-1 in hiPSC-CMs. BH3 mimetics targeting MCL-1 are promising anti-tumor therapeutics. Progression toward using BCL-2 family inhibitors, especially targeting MCL-1, depends on understanding its canonical function not only in preventing apoptosis but also in the maintenance of mitochondrial dynamics and function.

INTRODUCTION

Myeloid cell leukemia-1 (MCL-1) was originally identified as an early induced gene in human myeloid leukemia cell differentiation (Kozopas et al., 1993; Reynolds et al., 1996; Yang et al., 1996). MCL-1 is structurally similar to other anti-apoptotic BCL-2 (B cell lymphoma-2) family proteins (i.e. BCL-2, BCL-XL [B cell lymphoma extra-large]) (Chipuk et al., 2010). However, its larger, unstructured N-terminal domain and shorter half-life likely indicated that MCL-1 was not completely functionally redundant with other anti-apoptotic proteins (Perciavalle and Opferman, 2013). Supporting this idea, MCL-1 has been shown to be essential for embryonic development and for the survival of various cell types, including cardiomyocytes, neurons, and hematopoietic stem cells (Rinkenberger et al., 2000; Opferman et al., 2005; Arbour et al., 2008; Weber et al., 2010; Wang et al., 2013; Thomas et al., 2013).

MCL-1 is one of the most amplified genes in human cancers and is frequently associated with resistance to chemotherapy (Beroukhi et al., 2010; Perciavalle and Opferman, 2013). Earlier work demonstrated that MCL-1 genetic deletion is peri-implantation lethal in embryogenesis, not due to defects in apoptosis, but rather due to a combination of an embryonic developmental delay and an implantation defect (Rinkenberger et al., 2000). However, the nonapoptotic mechanism by which MCL-1 functions in normal and cancerous cells is still unclear. We previously reported that MCL-1 regulates mitochondrial dynamics in human pluripotent stem cells (hPSCs, which refer to both human embryonic stem cells [hESCs] and induced pluripotent stem cells [hiPSCs]) (Rasmussen et al., 2018). We found that MCL-1 maintains mitochondrial network homeostasis in hPSCs through interactions with dynamin-related protein 1 (DRP-1) and optic atrophy type 1 (OPA1), two GTPases responsible for maintaining mitochondrial morphology and dynamics. In this study, we investigated whether this nonapoptotic role of MCL-1 remains as stem cells differentiate, using cardiomyocytes derived from human-induced pluripotent stem cells (hiPSC-CMs).

Mitochondrial fusion promotes elongation of the mitochondrial network, which is key for mitochondrial DNA (mtDNA) homogenization and efficient assembly of the electron transport chain (ETC) (Westermann, 2010; Friedman and Nunnari, 2014). Loss of mitochondrial fusion has been implicated as a mechanism for the onset of dilated cardiomyopathy and reported to also contribute to hypertrophic cardiomyopathy and other heart diseases (Dorn, 2013; Dorn et al., 2015; Ong et al., 2017). Mitochondrial homeostasis is essential during cardiomyocyte differentiation and embryonic cardiac development (Kasahara et al., 2013; Kasahara

¹Department of Cell & Developmental Biology, Vanderbilt University, Nashville, TN 37232, USA

²Vanderbilt University Medical Center, Nashville, TN 37232, USA

³Vanderbilt Center for Stem Cell Biology, Vanderbilt University, Nashville, TN 37232, USA

⁴Vanderbilt Brain Institute, Vanderbilt University, Nashville, TN 37232, USA

⁵Vanderbilt Ingram Cancer Center, Vanderbilt University, Nashville, TN 37232, USA

⁶Vanderbilt Center for Arrhythmia Research and Therapeutics, Department of Medicine, Nashville, TN 37232, USA

⁷These authors contributed equally

⁸Lead Contact

*Correspondence: vivian.gama@vanderbilt.edu
<https://doi.org/10.1016/j.isci.2020.101015>



and Scorrano, 2014; Cho et al., 2014). However, there is limited information about the mechanisms used by cardiomyocytes to minimize the risks for apoptosis, especially in cells derived from highly sensitive stem cells (Imahashi et al., 2004; Murriel et al., 2004; Gama and Deshmukh, 2012; Dumitru et al., 2012; Walensky, 2012).

Ultrastructural changes in mitochondria have long been observed in response to alterations in oxidative metabolism (Hackenbrock, 1966; Khacho et al., 2016). It has become increasingly clear that individual mitochondrial shape changes can also have dramatic effects on cellular metabolism (Chan, 2007; Hsu et al., 2016; Itoh et al., 2013; Burté et al., 2015). Several studies in the heart suggest that alterations in mitochondrial dynamics cause abnormal mitochondrial quality control, resulting in the buildup of defective mitochondria and reactive oxygen species (ROS) (Galloway and Yoon, 2015; Song et al., 2017). Interestingly, it has been shown that modulating the production of ROS can favor or prevent differentiation into cardiomyocytes (Buggisch et al., 2007; Murray et al., 2014). Thus, specific metabolic profiles controlled by mitochondrial dynamics are likely critical for hiPSC-CMs, because they can influence cell cycle, biomass, metabolite levels, and redox state (Zhang et al., 2012).

It is not completely understood how dynamic changes in metabolism affect cardiomyocyte function. Deletion of MCL-1 in murine heart muscle resulted in lethal cardiomyopathy, reduction of mitochondrial DNA (mtDNA), and mitochondrial dysfunction (Thomas et al., 2013; Wang et al., 2013). Inhibiting apoptosis via concurrent BAK/BAX knockout allowed for the survival of the mice; conversely, the mitochondrial ultrastructure abnormalities and respiratory deficiencies were not rescued. These results indicate that MCL-1 also has a crucial function in maintaining cell viability and metabolic profile in cardiomyocytes. Despite these efforts, the nonapoptotic mechanism by which MCL-1 specifically functions in cardiomyocytes is still unknown. Furthermore, the role for MCL-1 in the regulation of mitochondrial dynamics in cardiac cells has not yet been defined. Here we report that MCL-1 inhibition via BH3 mimetics caused severe contractility defects and impaired long-term survival of hPSC-CMs, due to MCL-1's essential function regulating mitochondrial morphology and dynamics.

RESULTS

MCL-1 Inhibition Causes Severe Defects in hiPSC-CM Mitochondrial Network

Recently published small molecule inhibitors of MCL-1 have been anticipated as potent anti-tumor agents against MCL-1-dependent cancers with limited cardiotoxicity in mouse models (Cohen et al., 2012; Kotschy et al., 2016; Letai, 2016). Thus, we chose to use hiPSC-CMs to examine the effects of MCL-1 inhibition on mitochondrial morphology using the small molecule inhibitor S63845 (Kotschy et al., 2016), combined with structured illumination microscopy (SIM) to observe mitochondria at high resolution. Cardiomyocytes were imaged after 4 days of treatment with vehicle (DMSO) or MCL-1 inhibitor (S63845) and the caspase inhibitor Q-VD-OPh (QVD) to prevent downstream effects of apoptosis on mitochondrial morphology (Figures 1A–1C). Mitochondrial networks in S63845-treated cells were severely disrupted, with individual mitochondria becoming shorter in length and more globular on average, as opposed to elongated networks in control cells. Quantification of SIM images shows a significant reduction in average mitochondrial length (Figure 1D) and a significant increase in mitochondria sphericity (Figure 1E) compared with control cells. In addition to S63845, we also tested two other small molecule MCL-1 inhibitors, AMG-176 (AMG) and AZD5991 (AZD) (Caenepeel et al., 2018; Tron et al., 2018). Although we observed mitochondrial defects in both inhibitor conditions (Figures 1F–1H), mitochondrial morphology in AMG-treated cells was not significantly different compared with control cells (Figures 1I and 1J). Quantification of SIM images shows a significant reduction in average mitochondrial length in cells treated with AZD (Figure 1I).

Corresponding with the fragmented mitochondrial phenotypes seen in S63845-treated cells, we also observed impaired mitochondrial respiration as measured by the Seahorse XFe96 analyzer. MCL-1 inhibition significantly lowered the maximum oxygen consumption rate (OCR) after addition of FCCP, an uncoupler of oxidative phosphorylation (OXPHOS) (Figure S1A). ATP production was significantly reduced in S63845-treated cells as calculated from the OCR trace (Figure S1B). QVD was added to account for any effects on metabolism due to downstream apoptosis, but cells displayed similar OCR and ATP production as with S63845 alone (Figures S1C and S1D).

Recent reports have determined that MCL-1 functions not only as an apoptosis regulator but also as a modulator of mitochondrial morphology and dynamics (Perciavalle et al., 2012; Morciano et al., 2016;

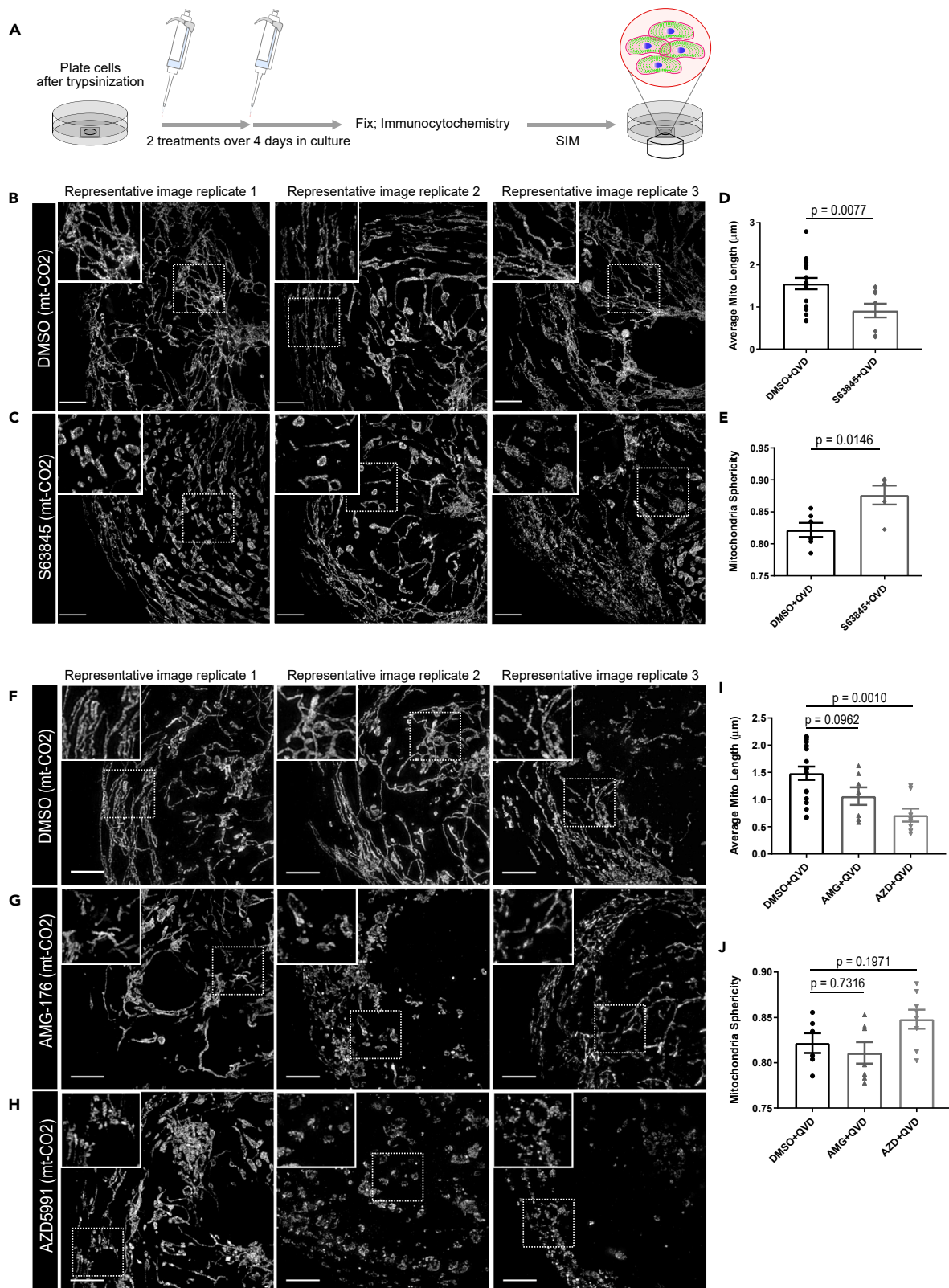


Figure 1. MCL-1 Inhibition Causes Mitochondrial Fragmentation

(A) Schematic of cell treatment paradigm used throughout this study. Structured Illumination Microscopy (SIM) was used for acquisition of all super-resolution images. hiPSC-CMs were treated with vehicle DMSO (B) or 2 μ M S63845 (C) and Q-VD-Oph (QVD). Quantification of average mitochondrial length (D) and mitochondrial sphericity (E) are shown, in which a spherical object would have a value of 1.0. hiPSC-CMs were treated with vehicle DMSO (F), 2 μ M AMG-176 (G), or 2 μ M AZD5991 (H) and QVD. Insets show magnification of individual mitochondria morphology. Scale: 5 μ m for all mitochondria images. Representative images are shown for all panels. Quantification of mitochondrial length (I) and mitochondrial sphericity (J) are shown, with AZD5991 treatment significantly decreasing average mitochondrial length. Graphs represent mean \pm SEM from at least three independent experiments ($n > 20$ cells per condition). See also Figure S1.

Rasmussen et al., 2018). Thus, we hypothesized that inhibiting MCL-1 with BH3 mimetics would affect the functionality of human cardiomyocytes, due to the disruption of crucial MCL-1 interactions with the mitochondrial dynamics machinery, which will ultimately lead to cell death.

MCL-1 Inhibition Affects Contractility of hiPSC-CMs and Myofibril Assembly in a Caspase-Independent Manner

Previous studies focused on human cardiomyocytes have suggested an effect of MCL-1 inhibition on mitochondrial morphology and mild effects on overall cardiac function (Guo et al., 2018). However, MCL-1 inhibition by S63845 was shown to have minimal effects on murine ejection fraction (Kotschy et al., 2016). These results are intriguing, considering previous studies reporting that MCL-1 deletion from murine cardiomyocytes has severe effects on mitochondrial morphology and cardiac function, which were not rescued by co-deletion of BAK and BAX (Wang et al., 2013). We treated hiPSC-CMs with S63845, while inhibiting caspase activity using QVD, and measured spontaneous cardiac beating using the AxionBiosystems analyzer (Clements and Thomas, 2014) (Figure 2A). We also used the BCL-2 inhibitor, Venetoclax (ABT-199) (Souers et al., 2013), to probe whether these cells are also sensitive to BCL-2 inhibition. We observed that only MCL-1 inhibition caused severe defects in cardiomyocyte functionality within 48 h of treatment (Figures 2B–2F). In particular, spike amplitude mean (Figure 2B) and spike slope mean (Figure 2C) were significantly decreased at 20 and 48 h, whereas beat period irregularity was significantly increased at 20 h post-treatment (Figure 2D). BCL-2 inhibition did not cause changes in cardiac beating ability compared with DMSO control in any of the measured parameters (Figures 2B–2F), suggesting that the function of hiPSC-CMs is highly dependent on MCL-1, but not BCL-2. S63845-treated cells stopped beating completely at 48 h, accounting for the decrease in beat period mean and beat period irregularity at this time point (Figures 2D and 2E). The field potential duration (FPD) was not detectable after 20 h of MCL-1 inhibition (Figure 2F). We also observed similar defects in cardiomyocyte functionality in cells treated with AZD, but not AMG (Figures S2A–S2E).

In a previous report, MCL-1 inhibition using RNAi also resulted in mitochondria morphology defects including severe cristae disruption and remarkable vacuolation in the mitochondrial matrix (Guo et al., 2018). In this study, MCL-1 knockdown by siRNA (Figures S2F and S2G) also caused increased beat period irregularity (Figure S2H), increased max delay mean (Figure S2I), and decreased FPD mean (Figure S2J). These results suggest that MCL-1 inhibition in human cardiomyocytes causes bradycardia- and arrhythmia-like phenotypes.

Because MCL-1 inhibition disrupted hiPSC-CM spike amplitude mean, we decided to probe whether calcium influx was also impaired in these cells. We visualized calcium dynamics using the GCaMP5G calcium reporter in hiPSC-CMs (Figure 2G). In DMSO-treated cells, we measured approximately a 1.9-fold increase in signal intensity (Figure 2H). As a positive control, we treated cells with cadmium chloride (CdCl_2), a calcium channel blocker, which completely disrupted calcium intake, giving a ratio of 1.0. Consistent with our results with the MEA recordings, calcium signal intensity was significantly reduced in hiPSC-CMs treated with S63845 or AZD. AMG treatment caused a significant, but less severe, reduction in calcium intake. We also measured beating by light microscopy and found that MCL-1 inhibition reduced the proportion of beating cells in a dose-dependent manner (Figure 2I).

Intriguingly, we also observed significant changes in the structure of the actin network and subsequent myofibril organization in cells treated with any of the MCL-1 inhibitors (Figures 2J and S2K). hiPSC-CMs treated with MCL-1 inhibitors displayed poor Z-line organization, lower density of F-actin, and increased presence of stress fibers. Blinded quantification of F-actin organization revealed that MCL-1-inhibitor-treated cells had significantly less organized myofibril structure (Figures 2J and S2K).

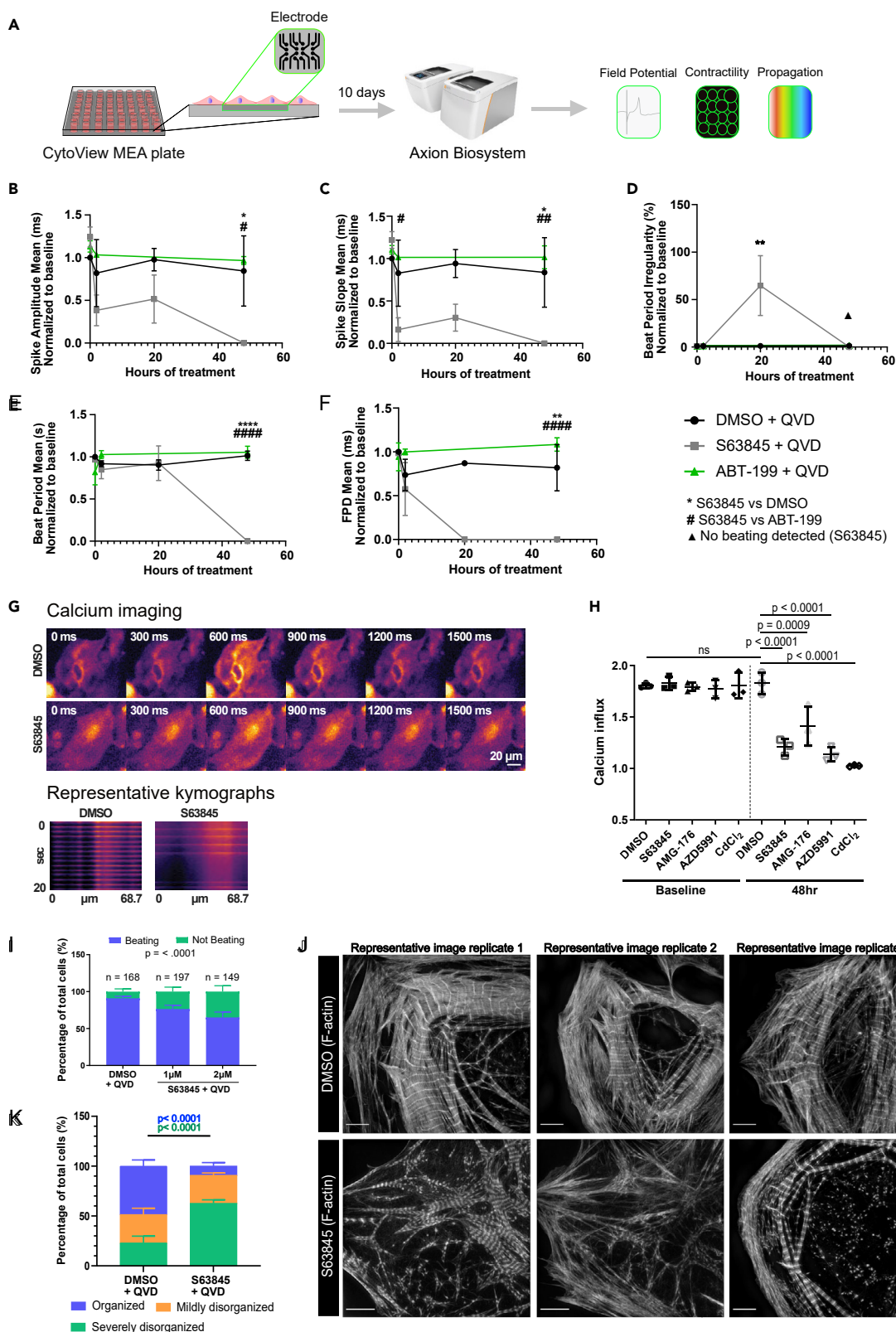


Figure 2. MCL-1 Inhibition Causes Functional Defects and Disruption of Myofibrils

(A–F) (A) Schematic of AxionBiosystems MEA paradigm for recording cardiac performance in live cells. hiPSC-CMs were plated on a CytoView MEA plate (AxionBiosystems) and treated with either vehicle (DMSO), 0.5 μ M S63845, or 0.5 μ M ABT-199 and QVD. Live-cell activity was recorded at baseline (0 h), 2 h, 20 h, and 48 h post-initial treatment for 5 min each. Spike amplitude mean (B) and spike slope mean (C) were both decreased by 20 h and completely reduced by 48 h in the S63845 condition. Beat period irregularity (D) was increased at 20 h in S63845-treated cells before cells stopped beating at 48 h, whereas DMSO and ABT-199 had low levels of beat period irregularity at 48 h. Beat period mean (E) remained at levels comparable to DMSO control before cells stopped beating at 48 h, whereas field potential duration (FPD) mean (F) was not detectable after 20 h. p values show significance as follows: * = DMSO + QVD versus S63845 + QVD, # = ABT-199 + QVD versus S63845 + QVD. One symbol indicates $p < 0.05$, two symbols indicate $p < 0.01$, three symbols indicate $p < 0.001$, and four symbols indicate $p < 0.0001$. p values were determined by two-way ANOVA. Graphs represent mean \pm SEM.

(G) Representative montage from GCaMP calcium indicator time-lapse imaging in hiPSC-CMs treated with DMSO + QVD or S63845 + QVD (top).

Representative kymographs of calcium pulses from individual cells treated with DMSO + QVD or S63845 + QVD (bottom).

(H) Quantification of calcium influx from hiPSC-CMs treated with QVD and either vehicle DMSO, S63845, AMG-176, or AZD5991, in which a value of 1.0 indicates no change in fluorescence intensity. $n = 60$ cells from three independent experiments. Symbols indicate mean and error bars indicate \pm SD.

(I) Proportion of beating versus not beating hiPSC-CMs in each condition as observed by light microscopy. Significance between beating versus not beating cells was determined by Chi-square test. Error bars indicate \pm SD and percentages were pooled from three experiments.

(J) Vehicle-treated hiPSC-CMs have organized myofibril structure as shown by maximum intensity projections. hiPSC-CMs treated with 2 μ M S63845 have myofibrils that are unorganized and poorly defined Z-lines. Scale: 5 μ m. Representative images are shown for all panels.

(K) Quantification of myofibril phenotypes represented in panel I ($n > 20$ cells per condition from three separate experiments). Error bars indicate \pm SD.

See also Figure S2.

MCL-1 Co-localizes with Mitochondrial Dynamics Proteins in hiPSC-CMs, and S63845 Disrupts MCL-1:DRP-1 Co-localization

Because MCL-1 inhibition disrupted mitochondrial network integrity in hiPSC-CMs and MCL-1 depletion affects mitochondrial dynamics proteins DRP-1 and OPA1 (Rasmussen et al., 2018), we next examined the effects of MCL-1 inhibition on the expression levels of these proteins in hiPSC-CMs. S63845-treated cells had a significant increase in the expression levels of DRP-1 (Figures 3A, 3B, and S3A–S3C) but not in phospho-DRP-1 (pDRP-1 S616) (Figure 3C). MCL-1 expression levels were significantly increased (Figures 3D and 3E). Previous studies also reported this induction of MCL-1 protein expression upon MCL-1 inhibition (Kotschy et al., 2016). There were no significant changes in OPA1 (Figures 3D and 3E) or TOM20 (Figures 3D and S3D). We then assessed whether MCL-1 interacts with DRP-1 and OPA1 using *in situ* proximity ligation assay (PLA). Our data show that MCL-1 is in close proximity to both DRP-1 and OPA1 (Figures 3G–3J). PLA puncta were quantified and normalized to the number of puncta in the control sample (no primary antibody) (Figure S3E). The co-localization of MCL-1 with DRP-1 (Figures 3G and 3H), but not OPA1 (Figures 3I and 3J), was disrupted upon inhibition of MCL-1 with S63845, suggesting that MCL-1 interacts with DRP-1 through its BH3-binding groove.

To further assess the disruption of the mitochondrial network caused by MCL-1 inhibition, we employed an assay using a photo-convertible plasmid (mito-tdEos) to assess connectivity and fusion/motility of mitochondria. After photo-converting an area of the mitochondrial network, we assessed the spread of red signal, which we used as a proxy for mitochondrial fusion. We observed that in cells treated with MCL-1 inhibitor, both the initial converted area and the spread of the converted red signal after 20 min were significantly decreased, indicating impaired mitochondrial fusion (Figures 4A–4D). This phenomenon was DRP-1 dependent, because cells deficient in DRP-1 maintained an elongated network even when treated with S63845 (Figures 4E, 4F, S4A, and S4B).

MCL-1 Inhibition Results in hiPSC-CM Death

To examine whether hiPSC-CMs treated with MCL-1 inhibitor were undergoing apoptosis, we treated the cells with increasing doses of S63845 and examined the activation of caspase-3 and caspase-7. Cells responded to S63845 in a dose-dependent manner after 48 h, with 1–2 μ M inducing the most caspase activity (Figure 5A). We observed a similar dose response with both AMG and AZD (Figure 5B). It is important to note that S63845 and AZD5991 have a similar chemical structure, and that these two inhibitors had more severe effects on cardiomyocytes overall (Hird and Tron, 2019). To confirm that cells were undergoing a caspase-dependent cell death, we performed long-term live cell imaging in the presence of MCL-1 inhibitors with and without caspase inhibition (Figures S4A–S4D). We observed similar levels of death regardless of caspase inhibition. These results indicate that hiPSC-CMs are also committing to a caspase-independent cell death in response to MCL-1 inhibition. To assess the type of death caused by MCL-1 inhibition, we treated the cells with IM-54, a known inhibitor of necrosis. IM-54 treatment rescued the toxicity caused by MCL-1 inhibition (Figure 5C).

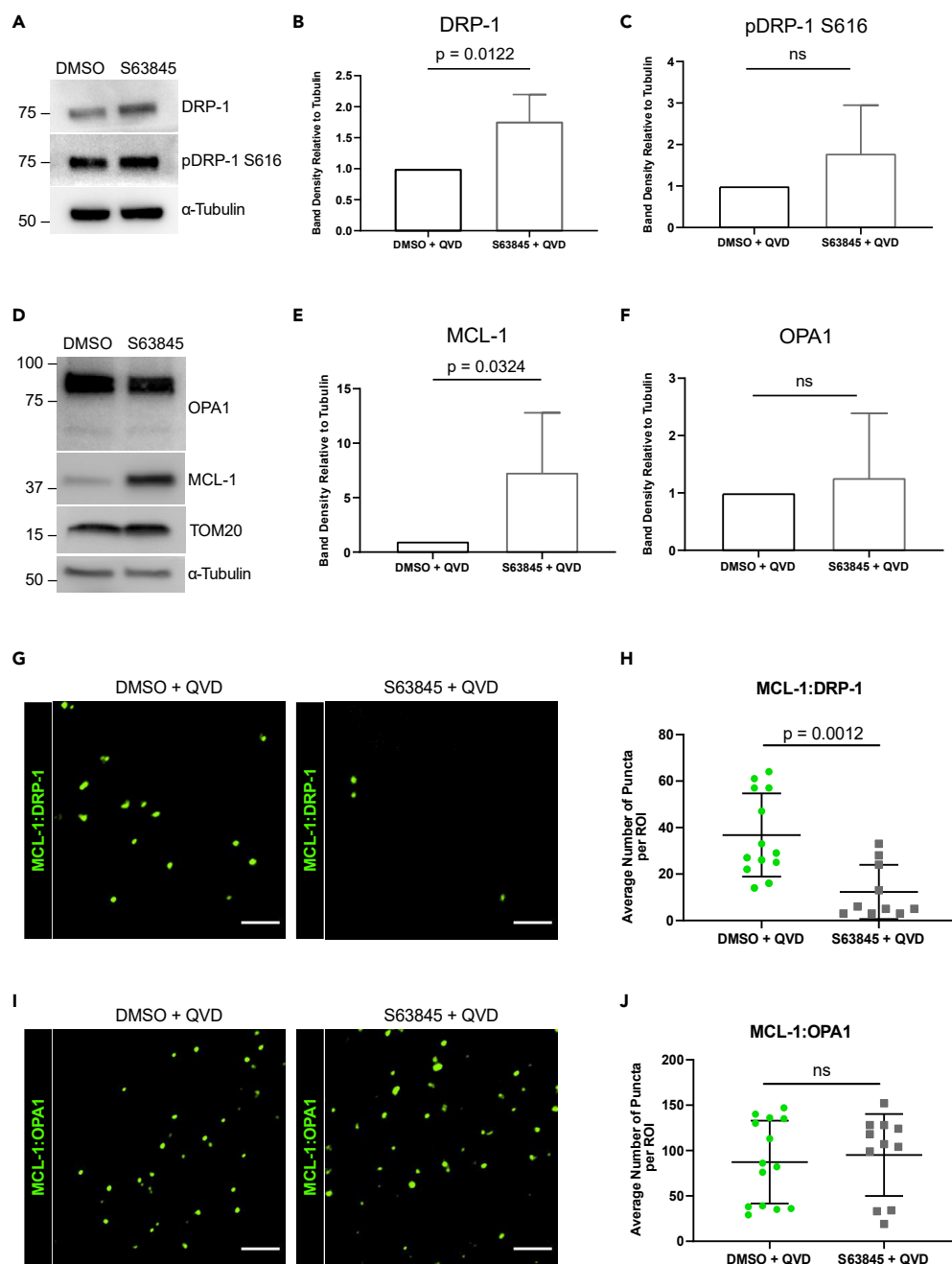


Figure 3. MCL-1 is in Close Proximity to Mitochondrial Dynamics Proteins

(A–C) (A) Western blot showing total and phospho-DRP-1 expression in hiPSC-CMs treated with DMSO + QVD or S63845 + QVD. Quantification of DRP-1 (B) and pDRP-1 S616 (C) band density relative to α -Tubulin (n = 3 independent experiments).

(D–F) (D) Western blot showing OPA1, MCL-1, and TOM20 levels in hiPSC-CMs treated with S63845 + QVD.

Quantification of MCL-1 (E) and OPA1 (F) band density relative to α -Tubulin (n = 3 independent experiments).

(G–J) Representative ROIs of PLA showing MCL-1:DRP-1 (G) or MCL-1:OPA1 (I) puncta in vehicle- or S63845-treated hiPSC-CMs. Scale: 5 μ m. Quantification of PLA puncta from MCL-1:DRP-1 (H) or MCL-1:OPA1 (J) interactions (n = 10–15 ROIs per condition from three independent experiments).

All graphs represent mean \pm SD. See also Figure S3.

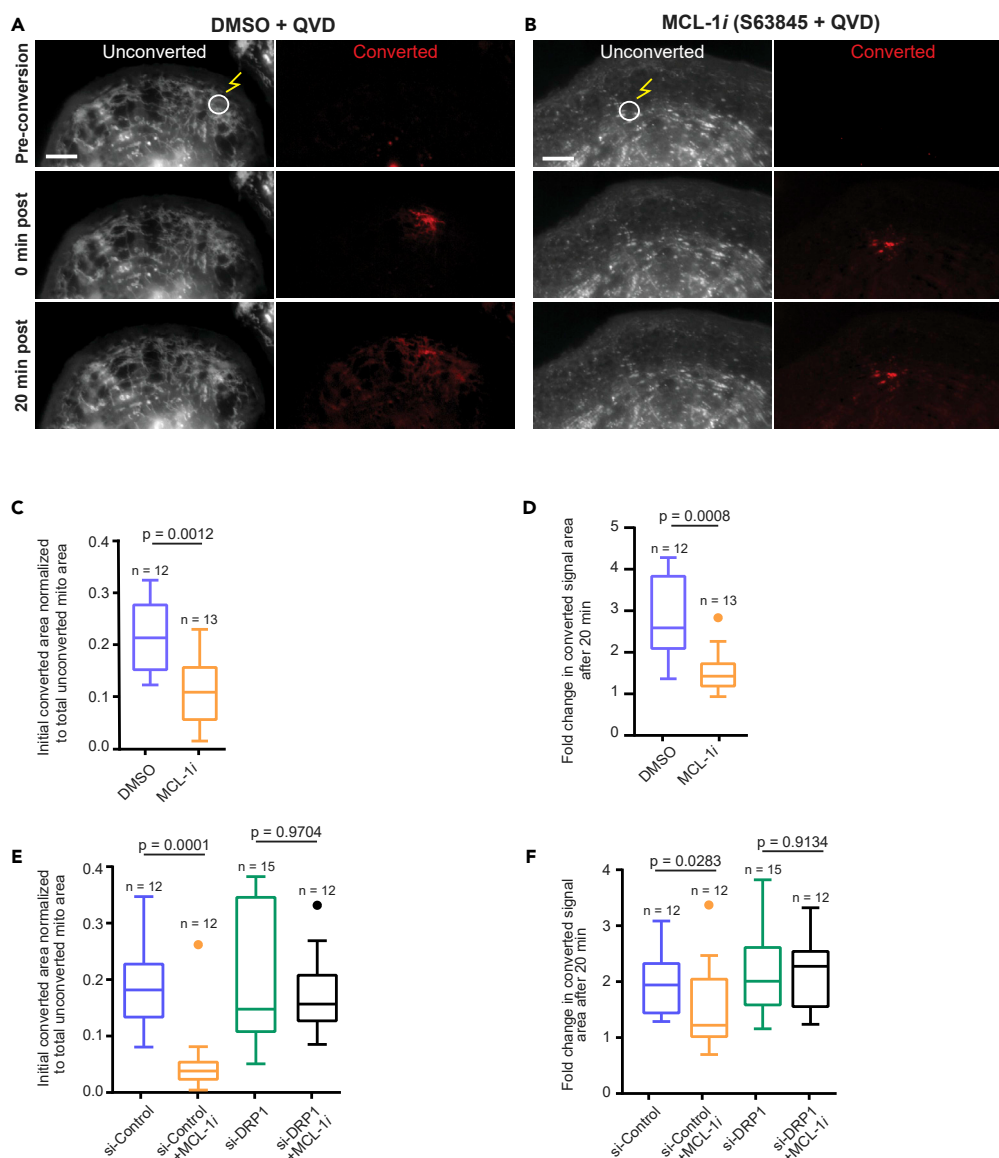


Figure 4. MCL-1 Inhibition Results in Mitochondrial Fragmentation in a DRP-1-Dependent Manner

(A–D) (A) Vehicle- and (B) S63845-treated hiPSC-CMs were transfected with mito-tdEos and a small area was photoconverted (see methods). Cells were imaged for 20 min post-conversion to assess mitochondrial network connectivity. Scale: 5 μ m. Quantification of the initial converted area normalized to total unconverted area (C) and fold change in converted area after 20 min (D) shows decreased initial connectivity and mitochondrial fusion after treatment with 2 μ M S63845 and QVD (MCL-1*i*).

(E) Quantification of initial converted area normalized to total unconverted area in hiPSC-CMs transfected with control siRNA or siRNA targeting DRP-1 \pm MCL-1*i* (2 μ M S63845) and QVD.

(F) Quantification of fold change in converted area after 20 min in same treatments from Figure 4E. Boxplots represent median of three independent experiments and Tukey whiskers.

See also Figure S4.

Previous reports have established that iPSC-derived cardiomyocytes mimic immature progenitor cells. To test the possibility that the effects of the MCL-1 inhibitors were exacerbated by the immature state of hiPSC-CMs, we used a previously published hormone-based method for cardiomyocyte maturation (Figures 6A and 6B) (Gentillon et al., 2019; Parikh et al., 2017). We tested for caspase-3/7 activation after 24 h of treatment with increasing doses of S63845 and detected similar effects of MCL-1 inhibition in hormone-matured hiPSC-CMs and vehicle-treated hiPSC-CMs (Figures 6C and 6D). Importantly, treatment

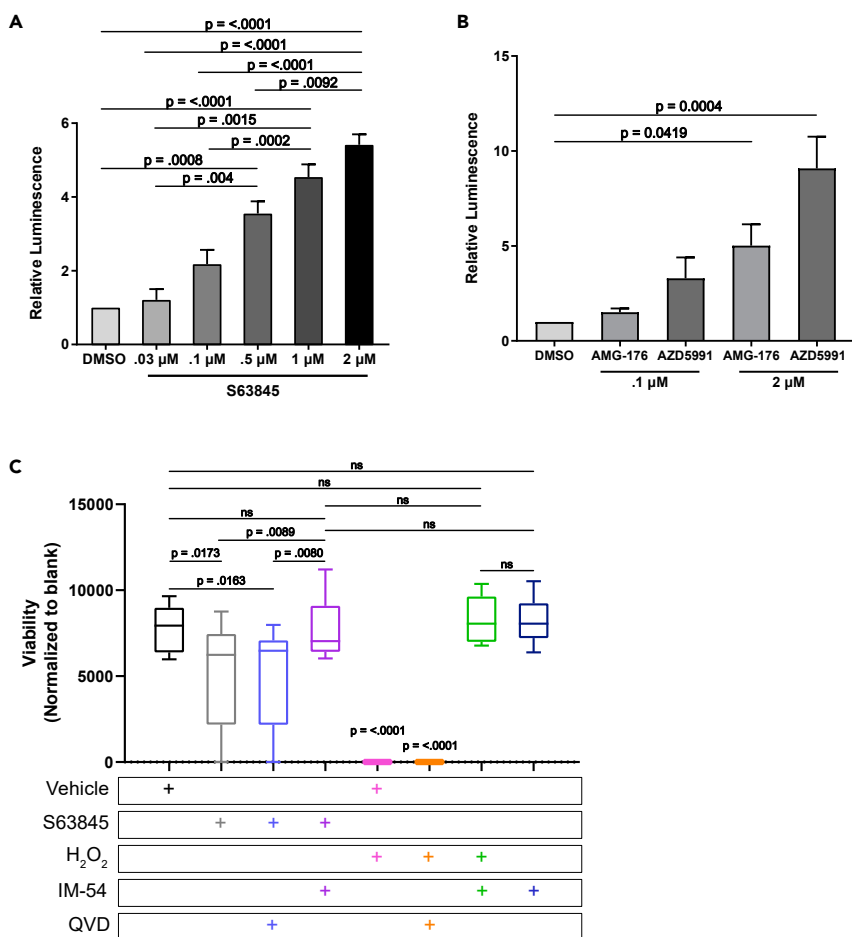


Figure 5. MCL-1 Inhibition Causes Cell Death in hiPSC-CMs that is Blocked by a Necrosis Inhibitor

(A and B) hiPSC-CMs were treated with increasing doses of S63845 (A) or AMG-176, and AZD5991 (B) for 48 h before caspase activity was measured by CaspaseGlo 3/7 assay (Promega). Quantification shows results from at least three independent experiments performed in duplicate and were normalized to DMSO control. Graphs represent mean \pm SEM.

(C) CellTiter-Blue assay (Promega) was used to assess cell viability in hiPSC-CMs. p values were calculated by one-way ANOVA. Data was quantified from three independent experiments performed in triplicate. Boxplots show median with Tukey whiskers.

See also Figure S5.

of these hormone-matured hiPSC-CMs also results in decreased functionality in response to a low dose of MCL-1 inhibitor (100 nM S63845) (Figures 6E–6G).

Long-term MCL-1 Inhibition, but Not BCL-2 Inhibition, Causes Defects in Cardiomyocyte Functionality

MCL-1 inhibition has significant effects on hiPSC-CM contractility and functionality when used at higher doses. To test if MCL-1 inhibition still affects cardiac functionality at lower doses, we treated hiPSC-CMs for two weeks (with treatments every two days) with 100 nM S63845. We also treated cells with the BCL-2 inhibitor ABT-199 (100 nM) and a combination of S63845 + ABT-199 (100 nM each). MCL-1 inhibition significantly disrupted hiPSC-CM spike amplitude mean and spike slope mean (Figures 7A and 7B). Although there were minimal differences between treatments in the beat period mean or FPD mean (Figures S6A and S6B), spike slope mean (Figure 7B), conduction velocity mean (Figure 7C), max delay mean (Figure 7D), and propagation consistency (Figure 7E) were significantly lowered in both the S63845 condition and when combined with ABT-199. Cells treated with ABT-199 appeared healthy and were functionally similar to control cells throughout the experiment (Figures 7A–7E, S6A, and S6B).

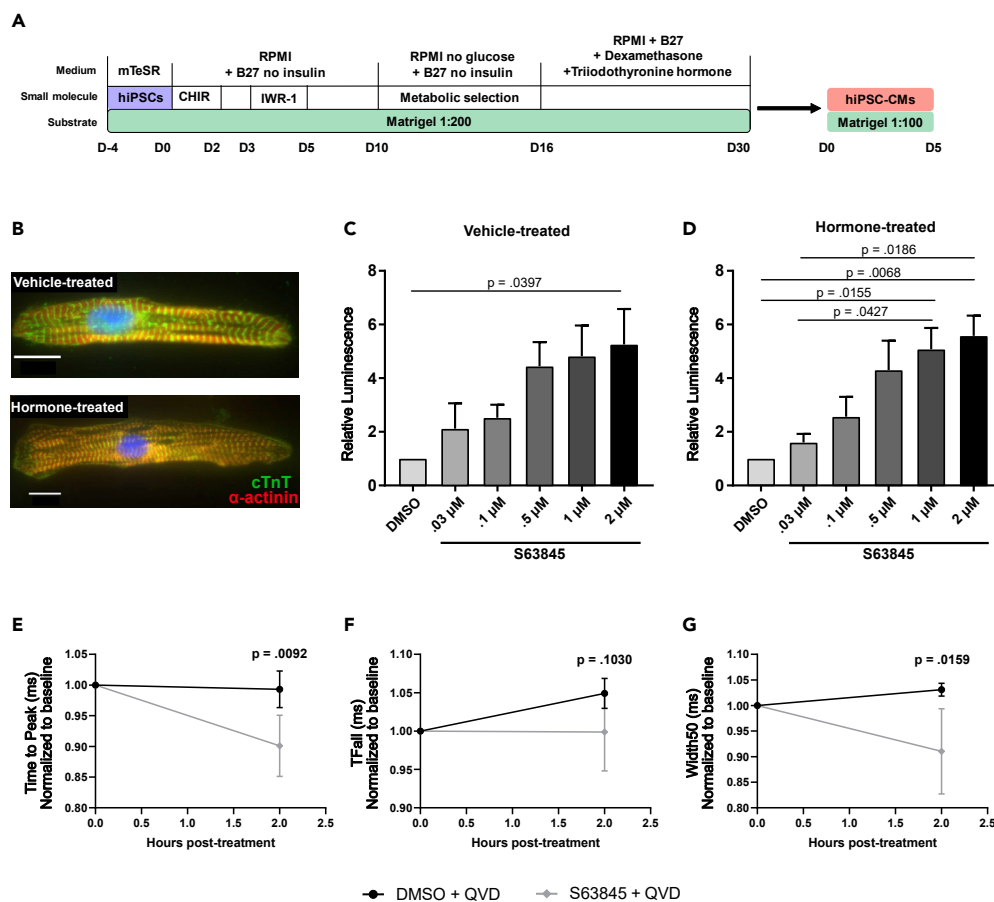


Figure 6. MCL-1 Inhibition Induces Caspase Activity and Reduces Functionality of Matured hiPSC-CMs

(A) Schematic of maturation protocol for hiPSC-CMs using triiodothyronine method.

(B) hiPSC-CMs treated with dexamethasone (Dex) and triiodothyronine (T3) display more mature myofibrillar phenotype compared with vehicle-treated control cells. Scale: 10 μ m.

(C and D) (C) Vehicle- or (D) Dex + T3-treated hiPSC-CMs were exposed to S63845 at increasing doses for 24 h. Caspase activity was measured as in Figures 5A and 5B using the CaspaseGlo 3/7 assay. Quantification was performed from three independent maturation experiments in duplicate. Graphs represent mean \pm SEM.

(E–G) CardioExcyte96 recordings show disruption of cardiac activity in Dex + T3-matured hiPSC-CMs when treated with 100 nM S63845. Data were quantified for Time to Peak (E), Time to Fall (TFall) (F), and Width50 (G). Quantification was performed from three independent maturation experiments for at least 5 wells per condition. p values were calculated by two-way ANOVA and graphs show mean \pm SEM.

Cells displayed mitochondrial network and actin disruption in the S63845-treated condition, and even more severe phenotypes were observed in cells treated with both inhibitors when compared with control cells (Figures 7F–7I and S6C–S6F). BCL-2 inhibition had little effect on mitochondrial network organization and virtually no effect on myofibrillar organization (Figures 7H and S6E). Our results further support the idea that MCL-1 is essential for maintaining mitochondrial homeostasis of human cardiomyocytes (Figure S7).

DISCUSSION

Recent studies have implicated MCL-1 in the maintenance of mitochondrial homeostasis in various cell types (Perciavalle and Opferman, 2013; Rasmussen et al., 2018; Senichkin et al., 2019). In this report, we show that MCL-1 inhibition affects human cardiomyocyte functionality potentially due to MCL-1's nonapoptotic role in modulating mitochondrial dynamics. Inhibition of MCL-1 using BH3 mimetics is a promising strategy to treat tumors (Hird and Tron, 2019), because resistance to chemotherapy is often associated with MCL-1 upregulation (Kotschy et al., 2016). To optimize the use of MCL-1 inhibitors, a deeper understanding of the biology of MCL-1 is crucial. Our studies show that MCL-1 inhibition affects

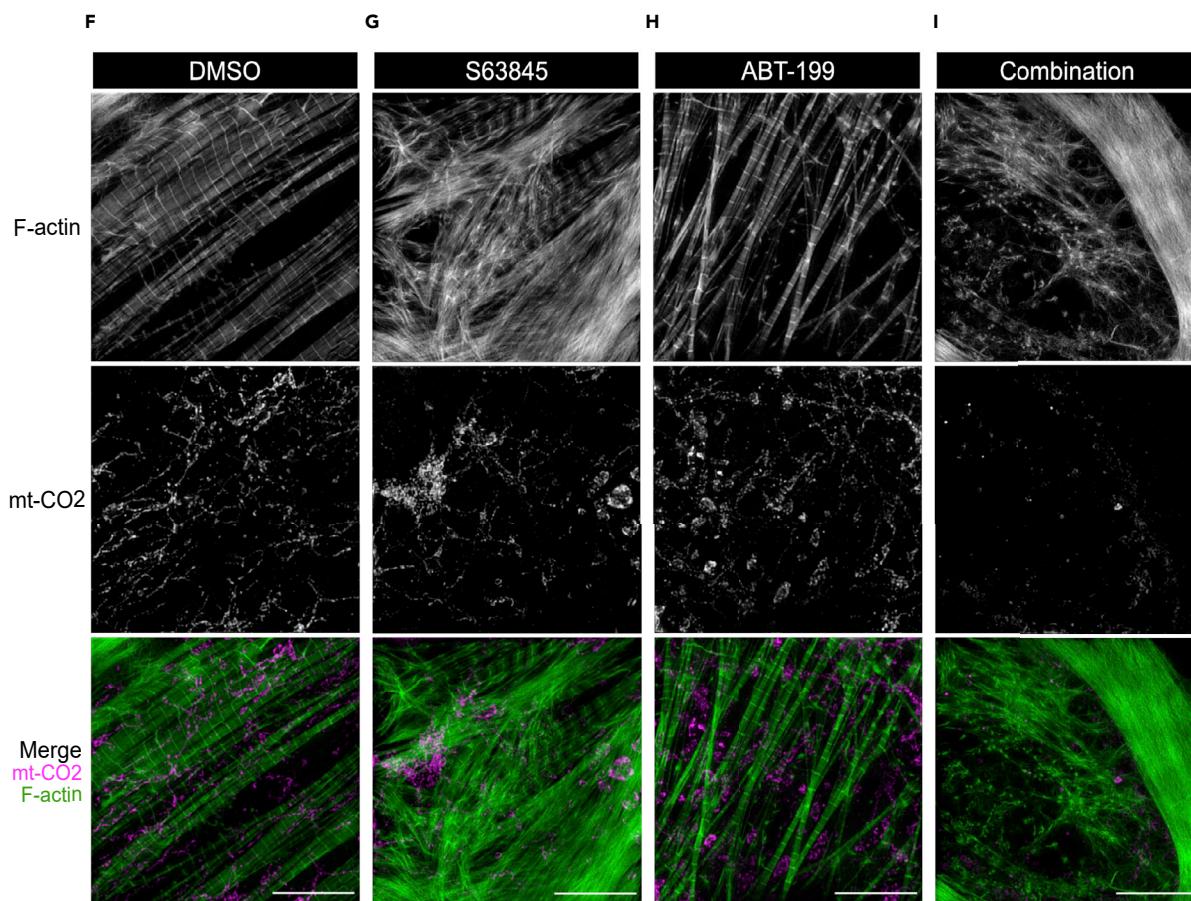
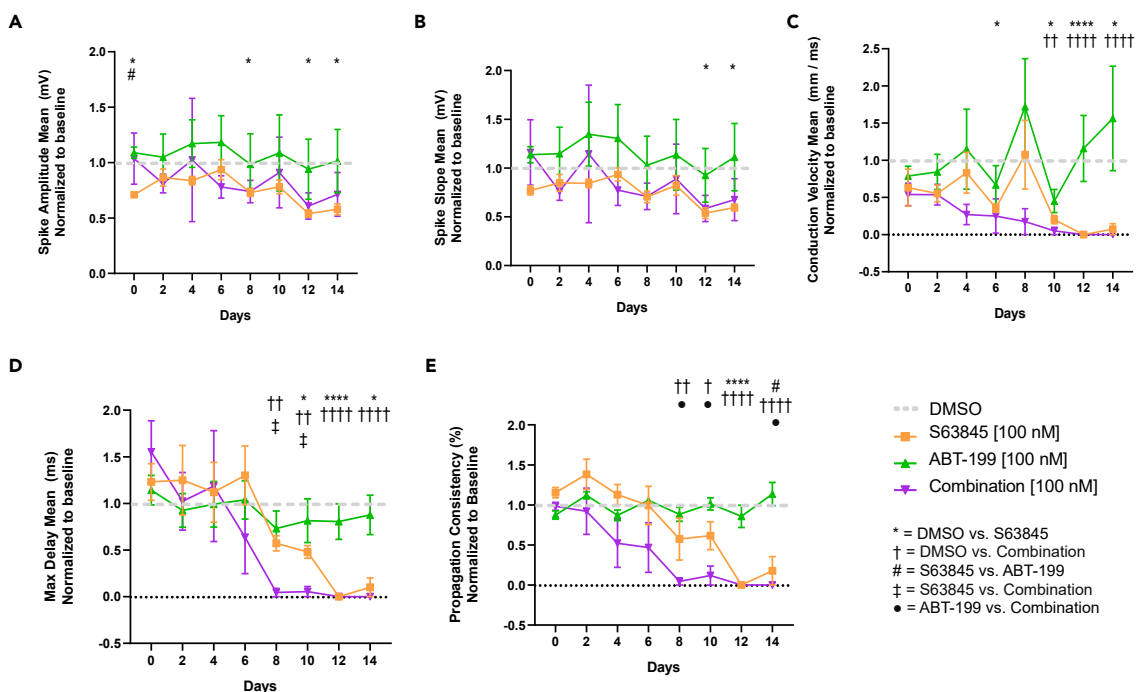


Figure 7. Long-term MCL-1 Inhibition Causes Defects in Functionality and Mitochondrial Morphology of hiPSC-CMs

(A–E) Chronic inhibition of MCL-1, but not BCL-2, results in cardiac activity defects. hiPSC-CMs were treated every 2 days with DMSO, 100 nM S63845 (orange), 100 nM ABT-199 (green), or both inhibitors (magenta) for 14 days. MEA recordings were taken 2 h following each treatment for 5 min, and results were normalized to baseline recording for each respective well, followed by normalization to DMSO (gray dotted line). Results of recordings for spike amplitude mean (A), spike slope mean (B), conduction velocity mean (C), max delay mean (D), and propagation consistency (E) are shown. p values show significance as follows: * = DMSO versus S63845, † = DMSO versus Combination, # = S63845 versus ABT-199, ‡ = S63845 versus Combination, ● = ABT-199 versus Combination. One symbol indicates $p < 0.05$, two symbols indicate $p < 0.01$, three symbols indicate $p < 0.001$, and four symbols indicate $p < 0.0001$. p values were determined by two-way ANOVA. Graphs represent mean \pm SEM.

(F–I) Mitochondria and F-actin were imaged at the end of the treatment paradigm in Figures 6A–6E. Representative images are shown of cells treated with DMSO (F), 100 nM S63845 (G), 100 nM ABT-199 (H), and 100 nM S63845 + 100 nM ABT-199 (Combination) (I). Scale: 10 μ m. See also Figure S6.

human cardiomyocyte functional parameters such as spike amplitude, beat propagation, and conduction velocity, which overlap with disruption of the mitochondrial and actin networks, ultimately leading to cell death.

Cardiomyocytes exposed to MCL-1 inhibitors appear to exhibit bradycardia and arrhythmia phenotypes. Interestingly, these phenotypes were not seen in cells treated with Venetoclax, indicating that hiPSC-CMs are less dependent on BCL-2 and highlighting a potential role for MCL-1 beyond its canonical function in apoptosis. This is further supported by the finding that hiPSC-CMs treated with 100 nM S63845 alone were alive, but not beating, after two weeks of treatment.

We hypothesize that this alternate function of MCL-1 in maintaining mitochondrial homeostasis is due to its interactions with DRP-1 and OPA1, which are essential regulators of mitochondrial morphology and dynamics (Labbé et al., 2014; Nishimura et al., 2018). Treatment of iPSC-CMs with MCL-1 inhibitor caused disruption of the mitochondrial network and significantly decreased MCL-1 proximity to DRP-1 at the mitochondria. Because the interaction with OPA1 was not disturbed, it is possible that MCL-1 interacts with OPA1 either through a different domain or with a different isoform of OPA1 in hiPSC-CMs than in hPSCs (Rasmussen et al., 2018). Another possibility is that, upon differentiation, the small molecule can no longer penetrate the inner mitochondrial membrane. We also confirmed that the mitochondrial network disruption is dependent on DRP-1, because DRP-1 knockdown prevented the fragmentation caused by MCL-1 inhibition. The recruitment of DRP-1 to the mitochondria has been proposed to be a critical inducer of mitophagy (Lee et al., 2011; Kageyama et al., 2014; Burman et al., 2017). Thus, an interesting possibility is that inhibition of MCL-1 is decreasing clearing of damaged mitochondria in cardiomyocytes. It will be important to test if key proteins involved in mitophagy are affected in the presence of MCL-1 inhibitors.

The photo-conversion experiments in this study did not test for fragmentation directly; thus it is possible that the mitochondrial phenotypes are caused by a lack of fusion or mitochondrial motility. Further studies into the mechanism of MCL-1's interaction with DRP-1 and OPA1 could shed light on this possibility. In contrast to iPSCs (Rasmussen et al., 2018), S63845 did not affect the proximity of MCL-1 with OPA1 at the mitochondria. MCL-1 at the mitochondrial matrix has been proposed to regulate β -oxidation of long fatty acids through interactions with VLCAD, and deletion of MCL-1 from the matrix caused hyperactivity of β -oxidation (Escudero et al., 2018). It is tempting to speculate that inhibiting MCL-1 at the matrix of human cardiomyocytes would result in significant damage to the heart.

We investigated the effects of MCL-1 inhibition on calcium flux using the GCaMP5G calcium reporter. Our data show a significant decrease in calcium flux with all inhibitors tested. These results could help explain the loss of functionality caused by MCL-1 inhibition. In addition to this loss of cardiomyocyte functionality, MCL-1 inhibition also caused significant disruption of actin networks within hiPSC-CMs. There are many possible mechanisms that could drive this phenotype. One hypothesis is that disruption of actin networks could be a result of decreased calcium flux and resultant loss of cardiomyocyte beating. Indeed, previous studies have shown that the maintenance of proper myofibril organization requires functional calcium channels and cellular contractility (Sharp et al., 1997; Simpson et al., 1993). Future studies should aim to test other potential hypotheses, such as altered metabolism and ROS production. Furthermore, cardiomyocytes treated with BH3 mimetics show a mild dose-dependent activation of caspase-3 that was inhibited by QVD. However, when measuring overall cell viability, the most significant rescue of viability was achieved by the necrosis inhibitor, IM-54. How is inhibition of MCL-1 triggering caspase-independent cell death that is blocked by this necrosis inhibitor? Mitochondrial disruption induced by BH3 mimetics may

cause increased oxidative stress that results in the loss of function and viability of cardiomyocytes. This is in agreement with a previous report (Thomas et al., 2013) that demonstrated the induction of necrosis in *Mcl-1*-deficient murine hearts. The data in this study showed that *Mcl-1* deletion did not result in the massive loss of myocytes due to apoptosis (Thomas et al., 2013). It would be of interest to examine the molecular mechanisms behind this phenotype.

MCL-1 inhibition also caused cardiomyocyte death in hormone-matured cells (Parikh et al., 2017). Although apoptotic sensitivity has been shown to decrease throughout development (Wright and Deshmukh, 2006; Sarosiek et al., 2017), these matured cells were more sensitive to S63845 treatment than vehicle-treated cells. It would be of interest to determine whether MCL-1 function in mitochondrial dynamics affects the maturation of iPSC-CMs or heart development *in vivo* (Kasahara et al., 2013; Feaster et al., 2015; Parikh et al., 2017). We speculate that other determinants of mitochondrial homeostasis, including mitochondrial biogenesis and mitophagy, may be affected by MCL-1 deficiency as cardiomyocytes mature. Although previous studies reported limited effects of S63845 on mouse heart function, a recent study using a humanized mouse model demonstrated that S63845 binds human MCL-1 with higher affinity than mouse MCL-1 (Kotschy et al., 2016; Brennan et al., 2018). Although this study did not report significant effects to the heart of humanized mice treated with S63845, the potential interactions of human MCL-1 with mitochondrial dynamics proteins and VLCAD may be species specific and not completely recapitulated in this mouse model. Collectively these reports highlight the importance of further research on the effect of MCL-1 on human-specific mitochondrial dynamics and metabolism. These results together with previous work from other groups (Thomas et al., 2013; Wang et al., 2013) suggest that hiPSC-CMs may be an appropriate platform to assess the safety and potential off-target effects of MCL-1 inhibitors on adult human hearts.

Studies from our laboratory suggest that inhibition of MCL-1 induces the differentiation of iPSCs (Rasmussen et al., 2018), which is likely associated with changes in metabolism to support cell-type-specific processes (Folmes et al., 2016). Because mitochondrial morphology is tightly coupled to metabolic adaptations, future studies will aim to investigate whether MCL-1 inhibition may cause a metabolic switch from fatty acid β -oxidation to glycolysis. Cardiac contractions depend on energy from these metabolic pathways, and thus cardiac mitochondria are forced to work constantly and likely require strict quality control mechanisms to maintain a functioning state (Dorn et al., 2015). This quality control process could depend in part on MCL-1. In support of this idea, our studies indicate that MCL-1 activity is essential for hiPSC-CM viability and contractility, which could be linked to MCL-1's nonapoptotic function at the mitochondrial matrix. The eventual apoptotic response detected at later time points could be the result of mitochondrial ROS signaling to trigger translocation and activation of BAX (Chaudhari et al., 2007). The disruption of actin and myofibril morphology could also be explained by heightened ROS induction and downstream ROS-mediated damage. Another important aspect that needs to be evaluated is the prevalence of phenotypically normal genetic variants that could predispose otherwise healthy individuals to stress-related cardiomyopathy (Garcia-Pavia et al., 2019). Our results emphasize the need for a more complete molecular understanding of MCL-1's mechanism of action in human cardiomyocytes, as it may reveal new approaches to prevent potential cardiac toxicities associated with chemotherapeutic inhibition of MCL-1.

Limitations of the Study

The protocol for myocyte maturation used in this study involves treatment with both tri-iodo-L-thyronine (T3) and dexamethasone, which leads to the generation of extensive T-tubule network and other functional traits of mature myocytes (Parikh et al., 2017). Although effective in generating "matured" T-tubule structures, we did not fully evaluate other traits of cardiomyocyte maturation. Thus, our study could be complemented by other approaches to achieve myocyte maturation (e.g. altering the metabolic state, co-culturing with mesenchymal stem cells, or using three-dimensional approaches) (Machiraju and Greenway, 2019; Karbassi et al., 2020). Collective data, however, suggest that MCL-1 activity is required for normal cardiac myocyte mitochondrial activity. The results reported here further support the validity for testing small molecule MCL-1 inhibitors in human iPSC-derived model systems that could reveal potential toxicity prior to admission in phase 1 clinical trials.

METHODS

All methods can be found in the accompanying [Transparent Methods supplemental file](#).

SUPPLEMENTAL INFORMATION

Supplemental Information can be found online at <https://doi.org/10.1016/j.isci.2020.101015>.

ACKNOWLEDGMENTS

We would like to thank Dr. Kevin Ess and John Snow for providing access and critical technical support with the AxionBiosystems MEA analyzer. We would also like to thank Dr. Ian Macara for providing access to the GloMax luminometer and Dr. Bryan Millis for providing expertise with high-resolution microscopy. This work was supported by 1R35 GM128915-01NIGMS (to VG), 4R00CA178190NCI (to VG), 1R21CA227483-01A1NCI (to VG), 19PRE34380515AHA (to MLR), 18PRE33960551AHA (to NT), 19POST34380182AHA (to LW), and R35 GM125028-01NIGMS (to DTB). The Vanderbilt Cell Imaging Shared Resource is supported by NIH grants 1S10OD012324-01 and 1S10OD021630-01. The authors declare no competing financial interests.

AUTHOR CONTRIBUTIONS

V. Gama, M. Rasmussen, and N. Taneja conceived the study, designed experiments, interpreted data, and wrote the manuscript. M. Rasmussen and N. Taneja designed and carried out all the cell biology experiments, with input from D. Burnette. A. Neiningner performed mitochondrial morphology analysis. L. Wang performed CM differentiation and maturation, and technical support was provided by A. Neiningner, G. Robertson, S. Riffle, and L. Shi. V. Gama designed and supervised the project. The manuscript was prepared by M. Rasmussen and V. Gama and revised by N. Taneja and D. Burnette. D. Burnette and B. Knollmann provided vital reagents and critical expertise.

DECLARATION OF INTERESTS

The authors declare no competing interests.

Received: September 13, 2019

Revised: February 25, 2020

Accepted: March 24, 2020

Published: April 24, 2020

REFERENCES

- Arbour, N., Vanderluit, J.L., Grand, J.N.L., Jahani-Asl, A., Ruzhynsky, V.A., Cheung, E.C.C., Kelly, M.A., MacKenzie, A.E., Park, D.S., Opferman, J.T., and Slack, R.S. (2008). Mcl-1 is a key regulator of apoptosis during CNS development and after DNA damage. *J. Neurosci.* **28**, 6068–6078.
- Beroukhi, R., Mermel, C.H., Porter, D., Wei, G., Raychaudhuri, S., Donovan, J., Baretina, J., Boehm, J.S., Dobson, J., Urashima, M., et al. (2010). The landscape of somatic copy-number alteration across human cancers. *Nature* **463**, 899–905.
- Brennan, M.S., Chang, C., Tai, L., Lessene, G., Strasser, A., Dewson, G., Kelly, G.L., and Herold, M.J. (2018). Humanized Mcl-1 mice enable accurate preclinical evaluation of MCL-1 inhibitors destined for clinical use. *Blood* **132**, 1573–1583.
- Buggisch, M., Ateghang, B., Ruhe, C., Strobel, C., Lange, S., Wartenberg, M., and Sauer, H. (2007). Stimulation of ES-cell-derived cardiomyogenesis and neonatal cardiac cell proliferation by reactive oxygen species and NADPH oxidase. *J. Cell Sci.* **120**, 885–894.
- Burman, J.L., Pickles, S., Wang, C., Sekine, S., Vargas, J.N.S., Zhang, Z., Youle, A.M., Nezich, C.L., Wu, X., Hammer, J.A., and Youle, R.J. (2017). Mitochondrial fission facilitates the selective mitophagy of protein aggregates. *J. Cell Biol.* **216**, 3231–3247.
- Burté, F., Carelli, V., Chinnery, P.F., and Yu-Wai-Man, P. (2015). Disturbed mitochondrial dynamics and neurodegenerative disorders. *Nat. Rev. Neurol.* **11**, 11–24.
- Caenepeel, S., Brown, S.P., Belmontes, B., Moody, G., Keegan, K.S., Chui, D., Whittington, D.A., Huang, X., Poppe, L., Cheng, A.C., et al. (2018). AMG 176, a selective MCL1 inhibitor, is effective in hematological cancer models alone and in combination with established therapies. *Cancer Discov.* **CD-18-0387**. <https://doi.org/10.1158/2159-8290.CD-18-0387>.
- Chan, D.C. (2007). Mitochondrial dynamics in disease. *N. Engl. J. Med.* **356**, 1707–1709.
- Chaudhari, A.A., Seol, J.-W., Kim, S.-J., Lee, Y.-J., Kang, H., Kim, I., Kim, N.-S., and Park, S.-Y. (2007). Reactive oxygen species regulate Bax translocation and mitochondrial transmembrane potential, a possible mechanism for enhanced TRAIL-induced apoptosis by CCCP. *Oncol. Rep.* **18**, 71–76.
- Chipuk, J.E., Moldoveanu, T., Llambi, F., Parsons, M.J., and Green, D.R. (2010). The BCL-2 family reunion. *Mol. Cell* **37**, 299–310.
- Cho, S.W., Park, J., Heo, H.J., Park, S., Song, S., Kim, I., Han, Y., Yamashita, J.K., Youm, J.B., Han, J., and Koh, G.Y. (2014). Dual modulation of the mitochondrial permeability transition pore and redox signaling synergistically promotes cardiomyocyte differentiation from pluripotent stem cells. *J. Am. Heart Assoc.* **3**, <https://doi.org/10.1161/JAHA.113.000693>.
- Clements, M., and Thomas, N. (2014). High-throughput multi-parameter profiling of electrophysiological drug effects in human embryonic stem cell derived cardiomyocytes using multi-electrode arrays. *Toxicol. Sci.* **140**, 445–461.
- Cohen, N.A., Stewart, M.L., Gavathiotis, E., Tepper, J.L., Bruekner, S.R., Koss, B., Opferman, J.T., and Walensky, L.D. (2012). A competitive stapled peptide screen identifies a selective small molecule that overcomes MCL-1-dependent leukemia cell survival. *Chem. Biol.* **19**, 1175–1186.
- Dorn, G.W. (2013). Mitochondrial dynamics in heart disease. *Biochim. Biophys. Acta* **1833**, 233–241.
- Dorn, G.W., Vega, R.B., and Kelly, D.P. (2015). Mitochondrial biogenesis and dynamics in the developing and diseased heart. *Genes Dev.* **29**, 1981–1991.

- Dumitru, R., Gama, V., Fagan, B.M., Bower, J.J., Swahari, V., Pevny, L.H., and Deshmukh, M. (2012). Human embryonic stem cells have constitutively active Bax at the Golgi and are primed to undergo rapid apoptosis. *Mol. Cell* 46, 573–583.
- Escudero, S., Zaganjor, E., Lee, S., Mill, C.P., Morgan, A.M., Crawford, E.B., Chen, J., Wales, T.E., Mourtada, R., Luccarelli, J., et al. (2018). Dynamic regulation of long-chain fatty acid oxidation by a noncanonical interaction between the MCL-1 BH3 helix and VLCAD. *Mol. Cell* 65, 729–743.e7.
- Feaster, T.K., Cadar, A.G., Wang, L., Williams, C.H., Chun, Y.W., Hempel, J.E., Bloodworth, N., Merryman, W.D., Lim, C.C., Wu, J.C., et al. (2015). Matrigel Mattress: a method for the generation of single contracting human-induced pluripotent stem cell–derived cardiomyocytes. *Circ. Res.* 117, 995–1000.
- Folmes, C.D., Ma, H., Mitalipov, S., and Terzic, A. (2016). Mitochondria in pluripotent stem cells: stemness regulators and disease targets. *Curr. Opin. Genet. Dev.* 38, 1–7.
- Friedman, J.R., and Nunnari, J. (2014). Mitochondrial form and function. *Nature* 505, 335–343.
- Galloway, C.A., and Yoon, Y. (2015). Mitochondrial dynamics in diabetic cardiomyopathy. *Antioxid. Redox Signal.* 22, 1545–1562.
- Gama, V., and Deshmukh, M. (2012). Human embryonic stem cells: living on the edge. *Cell Cycle Georget. Tex* 11, 3905–3906.
- Garcia-Pavia, P., Kim, Y., Restrepo-Cordoba, M.A., Lunde, I.G., Wakimoto, H., Smith, A.M., Toepfer, C.N., Getz, K., Gorham, J., Patel, P., et al. (2019). Genetic variants associated with cancer therapy-induced cardiomyopathy. *Circulation* 140, 31–41.
- Gentillon, C., Li, D., Duan, M., Yu, W.-M., Preiner, M.K., Jha, R., Rampoldi, A., Saraf, A., Gibson, G.C., Qu, C.-K., et al. (2019). Targeting HIF-1 α in combination with PPAR α activation and postnatal factors promotes the metabolic maturation of human induced pluripotent stem cell–derived cardiomyocytes. *J. Mol. Cell. Cardiol.* 132, 120–135.
- Guo, L., Eldridge, S., Furniss, M., Mussio, J., and Davis, M. (2018). Role of Mcl-1 in regulation of cell death in human induced pluripotent stem cell–derived cardiomyocytes in vitro. *Toxicol. Appl. Pharmacol.* 360, 88–98.
- Hackenbrock, C.R. (1966). Ultrastructural bases for metabolically linked mechanical activity in mitochondria. *J. Cell Biol.* 30, 269–297.
- Hird, A.W., and Tron, A.E. (2019). Recent advances in the development of Mcl-1 inhibitors for cancer therapy. *Pharmacol. Ther.* 198, 59–67.
- Hsu, Y.-H.R., Yogasundaram, H., Parajuli, N., Valtuille, L., Sergi, C., and Oudit, G.Y. (2016). MELAS syndrome and cardiomyopathy: linking mitochondrial function to heart failure pathogenesis. *Heart Fail. Rev.* 21, 103–116.
- Imahashi, K., Schneider, M.D., Steenbergen, C., and Murphy, E. (2004). Transgenic expression of Bcl-2 modulates energy metabolism, prevents cytosolic acidification during ischemia, and reduces ischemia/reperfusion injury. *Circ. Res.* 95, 734–741.
- Itoh, K., Nakamura, K., Iijima, M., and Sesaki, H. (2013). Mitochondrial dynamics in neurodegeneration. *Trends Cell Biol.* 23, 64–71.
- Kageyama, Y., Hoshijima, M., Seo, K., Bedja, D., Sysa-Shah, P., Andrabi, S.A., Chen, W., Höke, A., Dawson, V.L., Dawson, T.M., et al. (2014). Parkin-independent mitophagy requires Drp1 and maintains the integrity of mammalian heart and brain. *EMBO J.* 33, 2798–2813.
- Karbassi, E., Fenix, A., Marchiano, S., Muraoka, N., Nakamura, K., Yang, X., and Murry, C.E. (2020). Cardiomyocyte maturation: advances in knowledge and implications for regenerative medicine. *Nat. Rev. Cardiol.* 1–19, <https://doi.org/10.1038/s41569-019-0331-x>.
- Kasahara, A., Cipolat, S., Chen, Y., Dorn, G.W., and Scorrano, L. (2013). Mitochondrial fusion directs cardiomyocyte differentiation via calcineurin and notch signaling. *Science* 342, 734–737.
- Kasahara, A., and Scorrano, L. (2014). Mitochondria: from cell death executioners to regulators of cell differentiation. *Trends Cell Biol.* 24, 761–770.
- Khacho, M., Clark, A., Svoboda, D.S., Azzi, J., MacLaurin, J.G., Meghaizel, C., Sesaki, H., Lagace, D.C., Germain, M., Harper, M.-E., et al. (2016). Mitochondrial dynamics impacts stem cell identity and fate decisions by regulating a nuclear transcription program. *Cell Stem Cell* 19, 1–16.
- Kotschy, A., Szlavik, Z., Murray, J., Davidson, J., Maragno, A.L., Le Toumelin-Braizat, G., Chanrion, M., Kelly, G.L., Gong, J.-N., Moujalled, D.M., et al. (2016). The MCL1 inhibitor S63845 is tolerable and effective in diverse cancer models. *Nature* 538, 477–482.
- Kozopas, K.M., Yang, T., Buchan, H.L., Zhou, P., and Craig, R.W. (1993). MCL1, a gene expressed in programmed myeloid cell differentiation, has sequence similarity to BCL2. *Proc. Natl. Acad. Sci. USA* 5, 3516–3520.
- Labbé, K., Murley, A., and Nunnari, J. (2014). Determinants and functions of mitochondrial behavior. *Annu. Rev. Cell Dev. Biol.* 30, 357–391.
- Lee, Y., Lee, H.-Y., Hanna, R.A., and Gustafsson, Å.B. (2011). Mitochondrial autophagy by Bnip3 involves Drp1-mediated mitochondrial fission and recruitment of Parkin in cardiac myocytes. *Am. J. Physiol. Heart Circ. Physiol.* 301, H1924–H1931.
- Letai, A. (2016). S63845, an MCL-1 selective BH3 mimetic: another arrow in our quiver. *Cancer Cell* 30, 834–835.
- Machiraju, P., and Greenway, S.C. (2019). Current methods for the maturation of induced pluripotent stem cell–derived cardiomyocytes. *World J. Stem Cells* 11, 33–43.
- Morciano, G., Giorgi, C., Balestra, D., Marchi, S., Perrone, D., Pinotti, M., and Pinton, P. (2016). Mcl-1 involvement in mitochondrial dynamics is associated with apoptotic cell death. *Mol. Biol. Cell* 27, 20–34.
- Murray, T.V.A., Ahmad, A., and Brewer, A.C. (2014). Reactive oxygen at the heart of metabolism. *Trends Cardiovasc. Med.* 24, 113–120.
- Murriel, C.L., Churchill, E., Inagaki, K., Szveda, L.I., and Mochly-Rosen, D. (2004). Protein Kinase C δ activation induces apoptosis in response to cardiac ischemia and reperfusion damage. A mechanism involving Bad and the mitochondria. *J. Biol. Chem.* 279, 47985–47991.
- Nishimura, A., Shimauchi, T., Tanaka, T., Shimoda, K., Toyama, T., Kitajima, N., Ishikawa, T., Shindo, N., Numaga-Tomita, T., Yasuda, S., et al. (2018). Hypoxia-induced interaction of filamin with Drp1 causes mitochondrial hyperfission-associated myocardial senescence. *Sci. Signal.* 11, eaat5185.
- Ong, S.-B., Kalkhoran, S.B., Hernández-Reséndiz, S., Samangouei, P., Ong, S.-G., and Hausenloy, D.J. (2017). Mitochondrial-shaping proteins in cardiac health and disease – the long and the short of it! *Cardiovasc. Drugs Ther.* 31, 87–107.
- Opferman, J.T., Iwasaki, H., Ong, C.C., Suh, H., Mizuno, S., Akashi, K., and Korsmeyer, S.J. (2005). Obligate role of anti-apoptotic MCL-1 in the survival of hematopoietic stem cells. *Science* 307, 1101–1104.
- Parikh, S.S., Blackwell, D.J., Gomez-Hurtado, N., Frisk, M., Wang, L., Kim, K., Dahl, C.P., Fiane, A., Tønnessen, T., Kryshtal, D.O., et al. (2017). Thyroid and glucocorticoid hormones promote functional T-tubule development in human-induced pluripotent stem cell–derived cardiomyocytes. *Circ. Res.* 121, 1323–1330.
- Perciavalle, R.M., and Opferman, J.T. (2013). Delving deeper: MCL-1's contributions to normal and cancer biology. *Trends Cell Biol.* 23, 22–29.
- Perciavalle, R.M., Stewart, D.P., Koss, B., Lynch, J., Milasta, S., Bathina, M., Temirov, J., Cleland, M.M., Pelletier, S., Schuetz, J.D., et al. (2012). Anti-apoptotic MCL-1 localizes to the mitochondrial matrix and couples mitochondrial fusion to respiration. *Nat. Cell Biol.* 14, 575–583.
- Rasmussen, M.L., Kline, L.A., Park, K.P., Ortolano, N.A., Romero-Morales, A.I., Anthony, C.C., Beckermann, K.E., and Gama, V. (2018). A non-apoptotic function of MCL-1 in promoting pluripotency and modulating mitochondrial dynamics in stem cells. *Stem Cell Rep* 10, 684–692.
- Reynolds, J.E., Li, J., Craig, R.W., and Eastman, A. (1996). BCL-2 and MCL-1 expression in Chinese hamster ovary cells inhibits intracellular acidification and apoptosis induced by staurosporine. *Exp. Cell Res.* 225, 430–436.
- Rinkenberger, J.L., Horning, S., Klocke, B., Roth, K., and Korsmeyer, S.J. (2000). Mcl-1 deficiency results in peri-implantation embryonic lethality. *Genes Dev.* 6, 23–27.
- Sarosiek, K.A., Fraser, C., Muthalagu, N., Bhola, P.D., Chang, W., McBrayer, S.K., Cantlon, A., Fisch, S., Golomb-Mello, G., Ryan, J.M., et al. (2017). Developmental regulation of mitochondrial apoptosis by c-Myc governs age- and tissue-specific sensitivity to cancer therapeutics. *Cancer Cell* 31, 142–156.

Senichkin, V.V., Streletskaia, A.Y., Zhivotovsky, B., and Kopeina, G.S. (2019). Molecular comprehension of Mcl-1: from gene structure to cancer therapy. *Trends Cell Biol.* 29, 549–562.

Sharp, W.W., Simpson, D.G., Borg, T.K., Samarel, A.M., and Terracio, L. (1997). Mechanical forces regulate focal adhesion and costamere assembly in cardiac myocytes. *Am. J. Physiol. Heart Circ. Physiol.* 273, H546–H556.

Simpson, D.G., Decker, M.L., Clark, W.A., and Decker, R.S. (1993). Contractile activity and cell-cell contact regulate myofibrillar organization in cultured cardiac myocytes. *J. Cell Biol.* 123, 323–336.

Song, M., Franco, A., Fleischer, J.A., Zhang, L., and Dorn, G.W. (2017). Abrogating mitochondrial dynamics in mouse hearts accelerates mitochondrial senescence. *Cell Metab.* 26, 872–883.e5.

Souers, A.J., Levenson, J.D., Boghaert, E.R., Ackler, S.L., Catron, N.D., Chen, J., Dayton, B.D., Ding, H., Enschede, S.H., Fairbrother, W.J., et al. (2013). ABT-199, a potent and selective BCL-2

inhibitor, achieves antitumor activity while sparing platelets. *Nat. Med.* 19, 202–208.

Thomas, R.L., Roberts, D.J., Kubli, D.A., Lee, Y., Quinsay, M.N., Owens, J.B., Fischer, K.M., Sussman, M.A., Miyamoto, S., and Gustafsson, Å.B. (2013). Loss of MCL-1 leads to impaired autophagy and rapid development of heart failure. *Genes Dev.* 27, 1365–1377.

Tron, A.E., Belmonte, M.A., Adam, A., Aquila, B.M., Boise, L.H., Chiarparin, E., Cidado, J., Embrey, K.J., Gangl, E., Gibbons, F.D., et al. (2018). Discovery of Mcl-1-specific inhibitor AZD5991 and preclinical activity in multiple myeloma and acute myeloid leukemia. *Nat. Commun.* 9, 1–14.

Walensky, L.D. (2012). Stemming danger with golgified BAX. *Mol. Cell* 46, 554–556.

Wang, X., Bathina, M., Lynch, J., Koss, B., Calabrese, C., Frase, S., Schuetz, J.D., Rehg, J.E., and Opferman, J.T. (2013). Deletion of MCL-1 causes lethal cardiac failure and mitochondrial dysfunction. *Genes Dev.* 27, 1351–1364.

Weber, A., Boger, R., Vick, B., Urbanik, T., Haybaeck, J., Zoller, S., Teufel, A., Krammer, P., Opferman, J., Galle, P., et al. (2010). Hepatocyte-specific deletion of the anti-apoptotic protein Mcl-1 triggers proliferation and hepatocarcinogenesis in mice. *Hepatology* 51, 1226–1236.

Westermann, B. (2010). Mitochondrial fusion and fission in cell life and death. *Nat. Rev. Mol. Cell Biol.* 11, 872–884.

Wright, K.M., and Deshmukh, M. (2006). Restricting apoptosis for postmitotic cell survival and its relevance to cancer. *Cell Cycle* 5, 1616–1620.

Yang, T., Buchan, H.L., Townsend, K.J., and Craig, R.W. (1996). MCL-1, a member of the BCL-2 family, is induced rapidly in response to signals for cell differentiation or death, but not to signals for cell proliferation. *J. Cell. Physiol.* 166, 523–536.

Zhang, J., Nuebel, E., Daley, G.Q., Koehler, C.M., and Teitell, M.A. (2012). Metabolic regulation in pluripotent stem cells during reprogramming and self-renewal. *Cell Stem Cell* 11, 589–595.

Supplemental Information

MCL-1 Inhibition by Selective BH3 Mimetics Disrupts

Mitochondrial Dynamics Causing Loss of Viability

and Functionality of Human Cardiomyocytes

Megan L. Rasmussen, Nilay Taneja, Abigail C. Neininger, Lili Wang, Gabriella L. Robertson, Stellan N. Riffle, Linzheng Shi, Bjorn C. Knollmann, Dylan T. Burnette, and Vivian Gama

Supplemental Information Titles and Legends

Figure S1: Corresponding to Figure 1. Analysis of oxygen consumption in hiPSC-CMs treated with MCL-1 inhibitor. (A, C) Oxygen consumption rate (OCR) was measured using the Seahorse Biosciences Mito Stress Test on an XFe96 analyzer. OCR after injection of FCCP was significantly reduced in cells treated with S63845 only (A) and S63845 +QVD (C) compared to vehicle controls (n = 3 independent experiments done in triplicate). *p < .05, **p < .01, ***p < .001, and ****p < .0001. Error bars indicate \pm SEM. (B, D) ATP production was calculated from the corresponding OCR traces in panels A and C for each condition. ATP production was reduced in both conditions, with S63845 treatment alone resulting in significant impairment of ATP production compared to vehicle control (B). Graphs represent mean \pm SEM and p-values were determined by student's t-test.

Figure S2: Corresponding to Figure 2. (A) hiPSC-CMs were plated on a CytoView MEA plate (Axion Biosystems) and treated with QVD and vehicle (DMSO), 0.5 μ M AMG-176, or 0.5 μ M AZD5991. Live-cell activity was recorded for 5 minutes and results were normalized to baseline recordings for each well. Beat period irregularity (A) was increased at 18 hrs in AZD-treated cells before cells stopped beating at 48 hrs, while DMSO and AMG had low levels of beat period irregularity overall. Spike amplitude mean (B) and spike slope mean (C) were both decreased by 20 hrs and completely reduced by 48 hrs in the AZD condition. Propagation consistency (D) and field potential duration (FPD) (E) were both significantly reduced in AZD-treated cells at 20 hrs in comparison to DMSO control and AMG-176. P-values were determined by two-way ANOVA and show significance as follows: * = DMSO +QVD vs. AZD5991 +QVD, # = AZD5991 +QVD vs. AMG-176 +QVD. One symbol indicates p < 0.05, two symbols indicate p < 0.01, three symbols indicate p < 0.001, and four symbols indicate p < 0.0001. Graphs represent mean \pm SEM. (F) Schematic of MCL-1 knockdown experiments. hiPSC-CMs were plated from thaw in either the CytoView MEA plate or in a tissue culture-treated 96-well plate and fed regularly for 10 days,

followed by three rounds of siRNA transfection. Cells in the 96-well plate were lysed for Western blot following the third round of transfection. (G) Representative Western blot showing efficient knockdown of MCL-1 protein using siRNA. (H-J) Axion MEA recordings were taken as in panels A-E. Baseline recordings were taken at 0 days (pre-transfection), and subsequent recordings were taken at days 1, 3, 4, and 7 over the course of the knockdown paradigm depicted in panel F (n = 3 replicate experiments). MCL-1 knockdown resulted in higher beat period irregularity (H), higher maximum delay mean (I), and shorter FPD mean (J) compared to non-targeting control siRNA. *p <0.05, **p <0.01. Graphs indicate mean \pm SD. (K) Vehicle-treated hiPSC-CMs have organized myofibril structure as shown by maximum intensity projections. hiPSC-CMs treated with 2 μ M AMG-176 or 2 μ M AZD5991 have myofibrils that are unorganized and poorly defined Z-lines when compared to controls. Scale: 5 μ m. Representative images are shown for all panels. Quantification of myofibril phenotypes is shown (n > 20 cells per condition from 3 separate experiments). Error bars indicate \pm SD.

Figure S3: Corresponding to Figure 3. (A) Representative Western blot showing cytosolic fraction and membrane fractions from hiPSC-CM protein lysates treated with vehicle or S63845 and QVD. Quantification of DRP-1 signal intensity normalized to either α -Tubulin for the cytosolic fraction (B) or VDAC for the membrane fraction (C). Western blots from 3 independent experiments were quantified and graphs represent mean \pm SD. (D) Quantification for TOM20 band density from the experiment shown in Figure 3C. Graph represents mean \pm SD. (E) Representative image of secondary PLA probe control sample. The area around the nucleus was avoided for all quantification purposes. Scale: 20 μ m.

Figure S4: Corresponding to Figure 4. (A) Schematic of DRP-1 knockdown experiment followed by photo-conversion of mito-tdEos corresponding to Figure 4E-F. (B) Representative

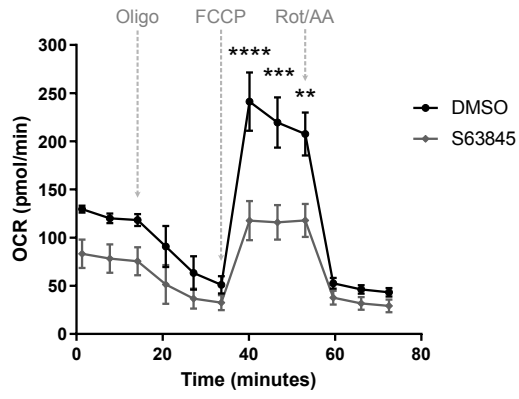
Western blot showing knockdown of DRP-1 compared to control siRNA corresponding to Figure 4E-F.

Figure S5: Corresponding to Figure 5. hiPSC-CMs were treated with S63845 at the indicated concentrations and either vehicle DMSO (A) or with QVD (B). Cell survival was measured over 4 days using an IncuCyte live cell imaging system. Representative images from each day of treatment were quantified and percentages of live cells are shown normalized to day 0 baseline. Graphs represent mean \pm SEM and experiments were performed in 4 independent replicates. (C) hiPSC-CMs were treated with the indicated concentrations of AMG-176 or AZD5991 and vehicle DMSO (C) or QVD (D). Cell survival was measured and quantified as in panels A-B. Graphs represent mean \pm SEM and experiments were performed in 3 independent replicates.

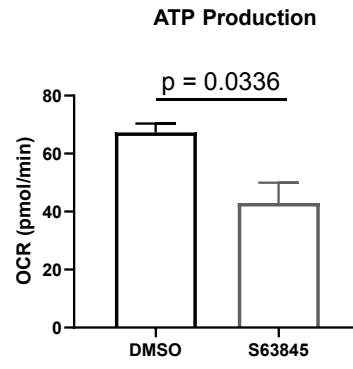
Figure S6: Corresponding to Figure 7. Chronic inhibition of MCL-1, but not BCL-2, results in cardiac activity defects. hiPSC-CMs were treated every 2 days with DMSO, 100 nM MCL-1i (S63845 - orange), 100 nM BCL-2i (ABT-199 - green), or both inhibitors (magenta) for 14 days. MEA plate was recorded 2 hours following each treatment for 5 minutes and results were normalized to baseline recording for each respective well, followed by normalization to DMSO (gray dotted line). Results of recordings for beat period mean (A) and field potential duration mean (B) are shown. P-values were calculated by two-way ANOVA and show significance as follows: * = DMSO vs. S63845, † = DMSO vs. Combination, # = S63845 vs. ABT-199, ‡ = S63845 vs. Combination, ● = ABT-199 vs. Combination. One symbol indicates $p < 0.05$, two symbols indicate $p < 0.01$, three symbols indicate $p < 0.001$, and four symbols indicate $p < 0.0001$. Error bars indicate \pm SEM. (F-I) Mitochondria and F-actin were imaged at the end of the treatment paradigm in Figure 6A-E. Representative SIM images are shown of cells treated with DMSO (F), 100 nM S63845 (G), 100 nM ABT-199 (H), and 100 nM S63845 + 100 nM ABT-199 (Combination) (I). Scale: 10 μ m.

Figure S7: Corresponding to Figure 1- Figure 7. Main findings in the study.

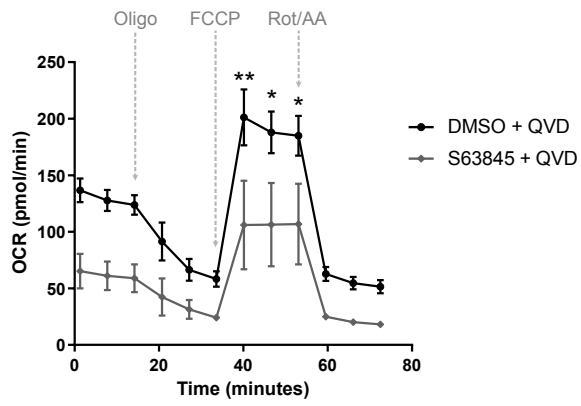
A



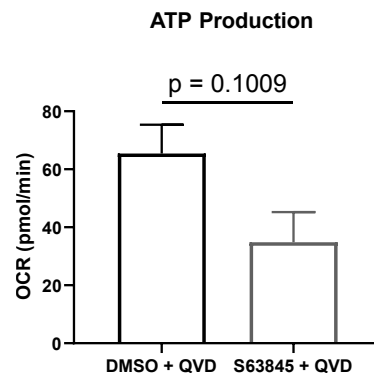
B



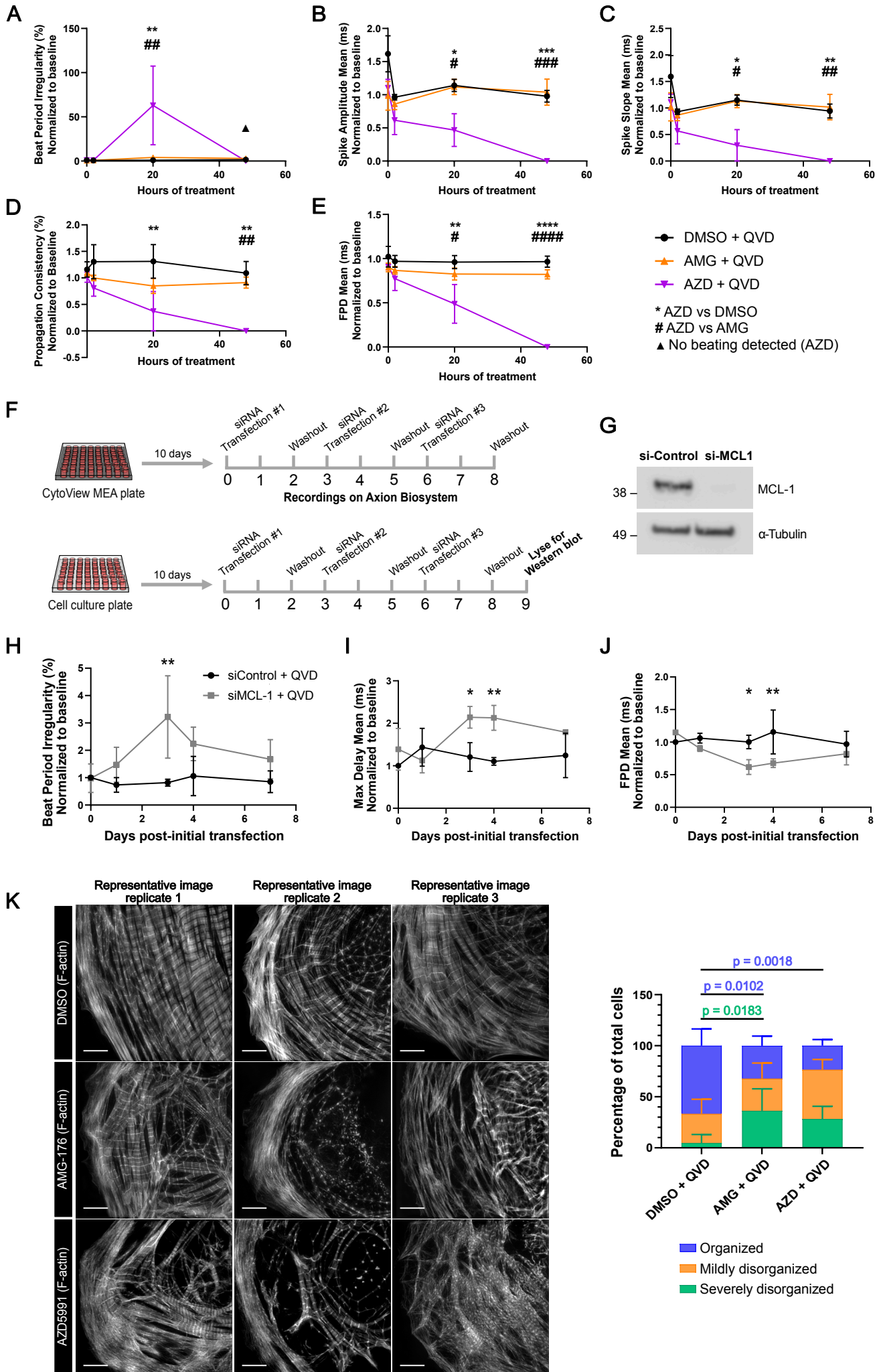
C



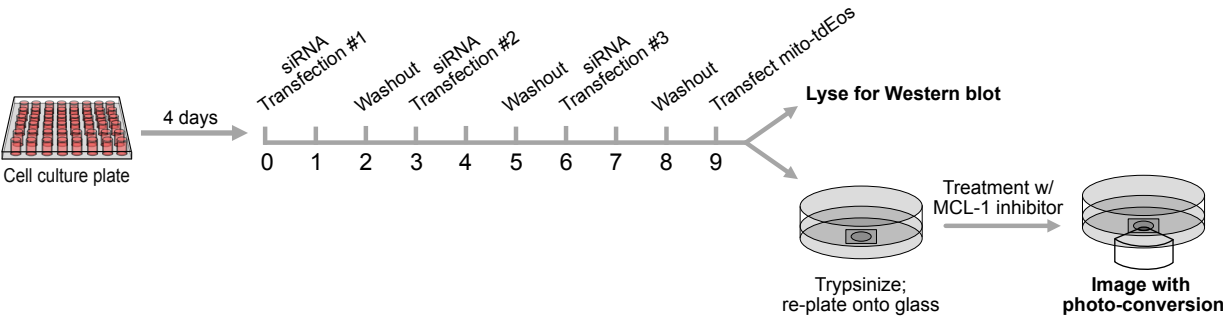
D



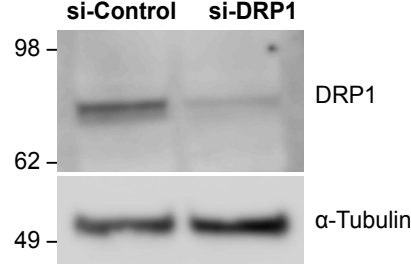
Supplemental Figure 2

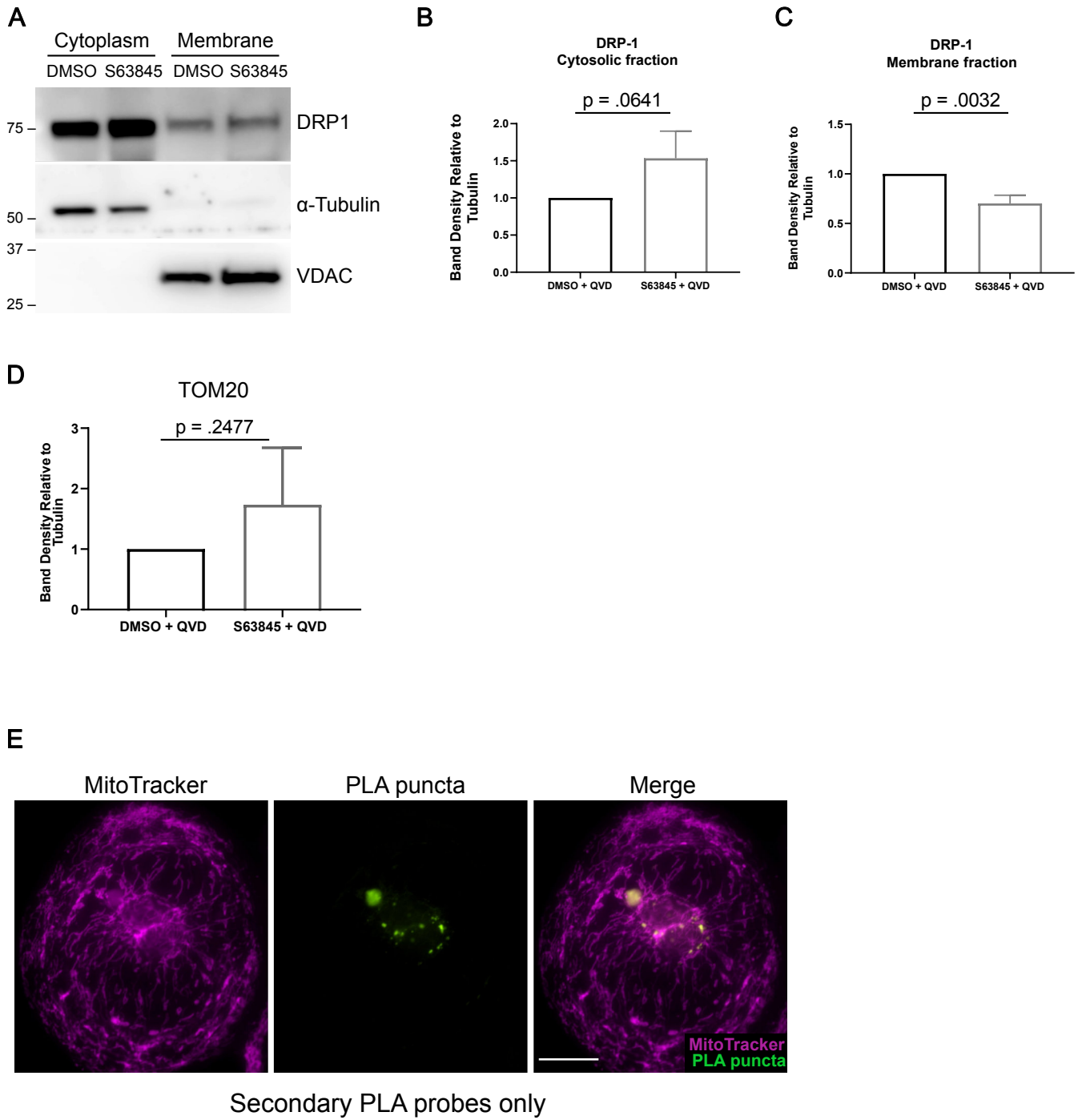


A

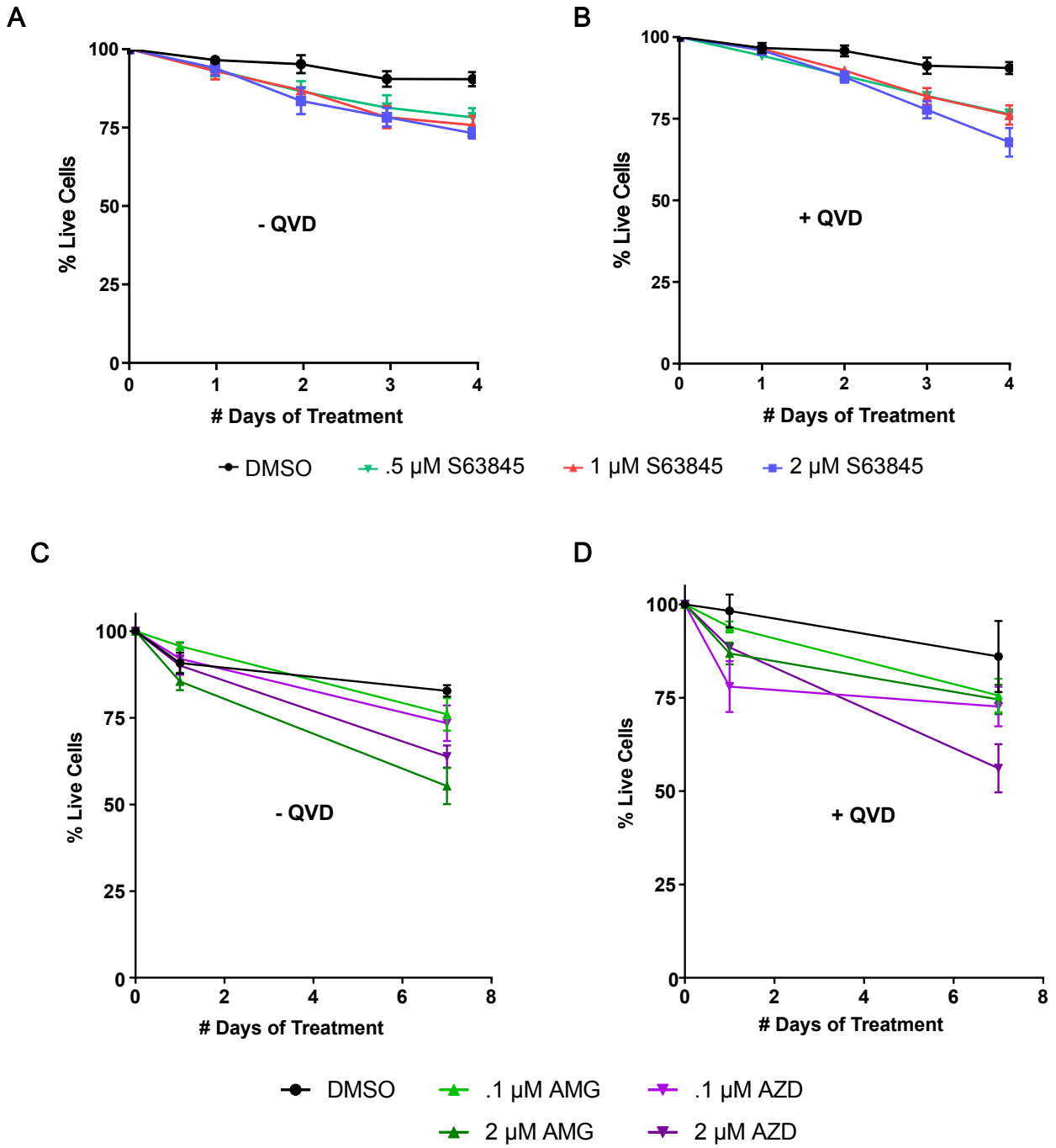


B

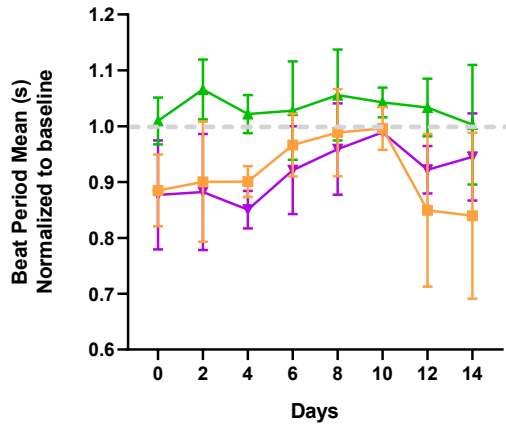




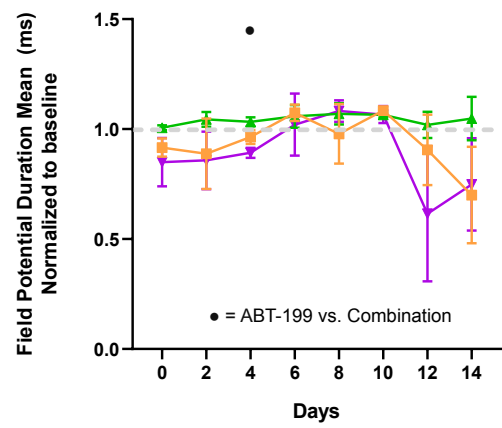
Supplemental Figure 5



A



B



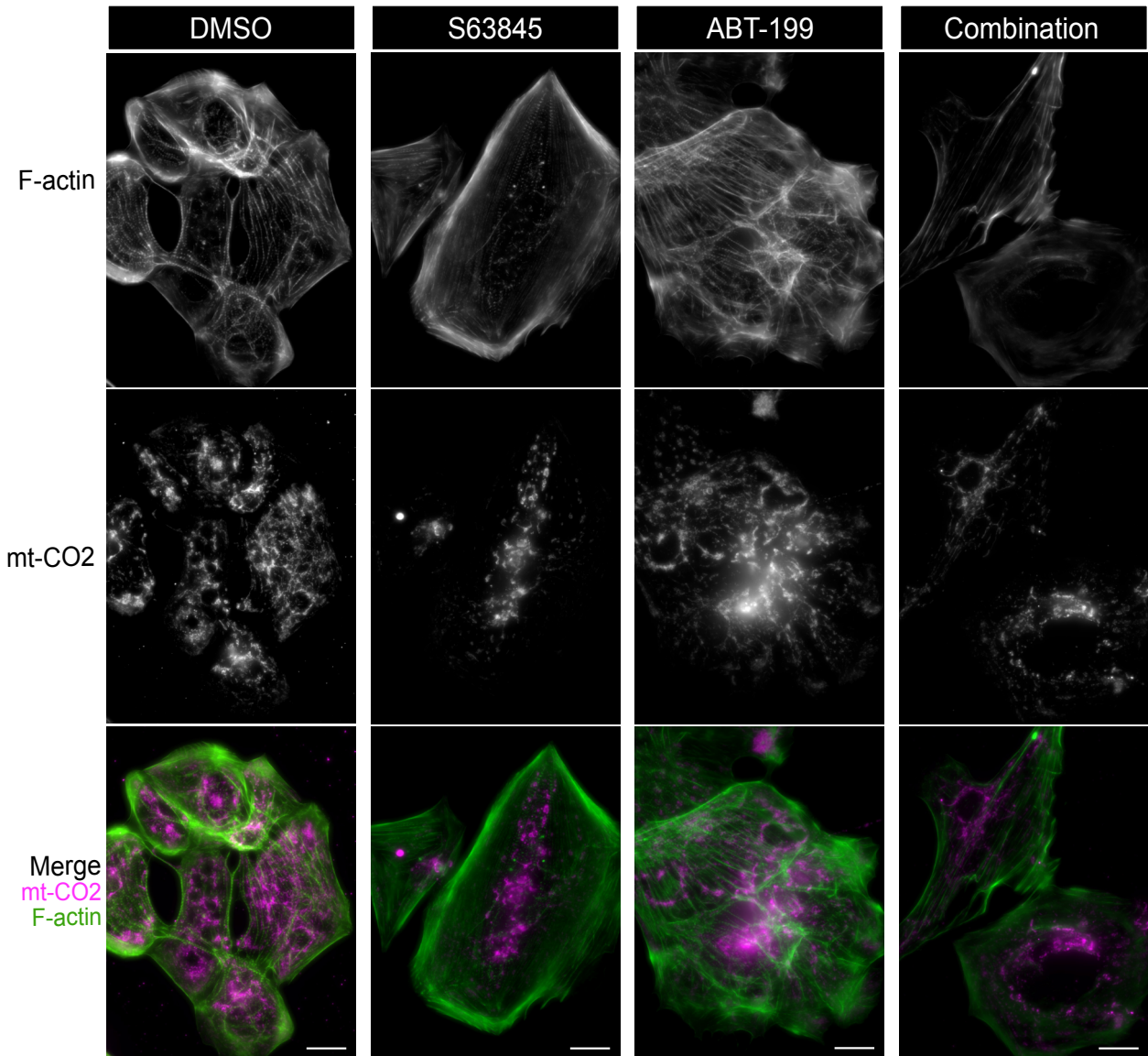
--- DMSO ■ S63845 [100 nM] ▲ ABT-199 [100 nM] ▼ Combination [100 nM]

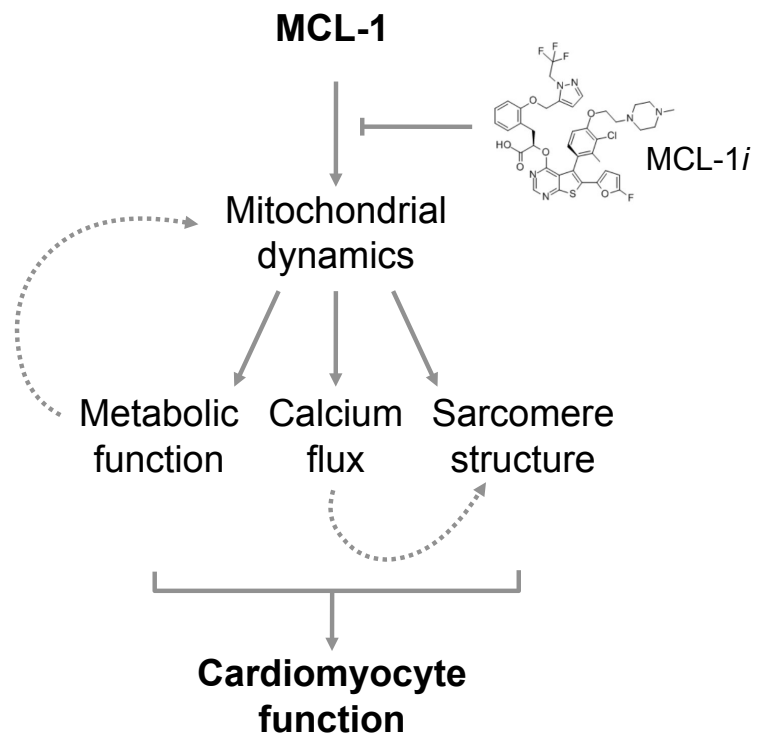
C

D

E

F





Materials and Methods

Cell Culture

Human induced pluripotent stem cell-derived cardiomyocytes (iCell Cardiomyocytes²) were obtained from Cellular Dynamics International (#CMC-100-012-000.5). Cells were thawed according to the manufacturer protocol in iCell Plating medium. Briefly, cells were thawed and plated on 0.1% gelatin at 50,000 cells/well in 96-well plates. Cells were maintained at 37°C and 5% CO₂ and fed every other day with iCell Cardiomyocyte Maintenance medium (Cellular Dynamics International #M1003). For knockdown experiments, wells were coated with 5 µg/mL fibronectin (Corning #354008) 1 hour prior to plating. For functional experiments using the Axion bioanalyzer, cells were plated on 50 µg/mL fibronectin in a 48-well CytoView MEA plate (Axion Biosystems #M768-tMEA-48B). For imaging experiments, cells were re-plated on glass-bottom 35 mm dishes (Cellvis #D35C4-20-1.5-N) coated with 10 µg/mL fibronectin. For live-cell imaging, cells were maintained at 37°C with 5% CO₂ in a stage top incubator (Tokai Hit). To account for batch effects, at least two different vials of iCell Cardiomyocytes² were used to replicate each experiment.

Human induced pluripotent stem cells (hiPSC) were generated from human fibroblasts as previously described (Wang et al., 2018). hiPSCs were maintained on growth factor-reduced Matrigel (Corning) coated plates in home-made E8 medium. hiPSCs were passaged every 4 days using 0.5 mM EDTA for 10 minutes at room temperature. hiPSCs were maintained at 37 °C at 5% CO₂ and received fresh medium daily.

hiPSC-derived cardiomyocytes (hiPSC-CMs) used in Figure 6 were generated using the small molecules CHIR 99021 (Selleck Chemicals) and IWR-1 (Sigma). Cardiac differentiation media were defined as M1 (RPMI 1640 with glucose with B27 minus insulin), M2 (RPMI 1640 minus glucose with B27 minus insulin), and M3 (RPMI 1640 with glucose with B27). hiPSCs were cultured until they reached 60% confluence, at which point cardiac differentiation was initiated (day 0). At day 0, hiPSCs were supplemented in M1 with 6 µM CHIR99021. On day 2, the media

was changed to M1. On day 3, cells were treated with 5 μ M IWR-1 in M1. Metabolic selection was started at day 10 and cells were treated with M2 from day 10 to 16. On day 16, cells were transitioned to M3 with or without 0.1 μ M triiodo-L-thyronine hormone (Sigma) and 1 μ M Dexamethasone (Cayman) (Parikh et al., 2017). Media was changed every other day until day 30. For experiments in Figure 5, data was collected from at least three separate differentiations.

Cell Treatments

All treatments were added directly to cells in maintenance medium. The pan-caspase inhibitor Q-VD-OPh (SM Biochemicals #SMPH001) was added to cells at a concentration of 25 μ M. The small molecule MCL-1 inhibitor derivative (S63845) was a gift from Joseph Opferman (St. Jude's Children Hospital). ABT-199 was purchased from Active Biochemicals (#A-1231). AMG-176 (#CT-AMG176) and AZD5991 (#CT-A5991) were purchased from ChemieTek. The necrosis inhibitor IM-54 (#SC222053A) was purchased from Santa Cruz Technologies and added to cells at a concentration of 10 μ M. All stock solutions were prepared in DMSO. H₂O₂ solution (#H1009) was purchased from Sigma and added to cells at 10 μ M in sterile water.

RNAi and Plasmid Transfection

Commercially available siRNAs targeting DRP-1 (DNM1L) (Thermo Fisher Scientific #AM51331, ID19561) and MCL-1 (Thermo Fisher Scientific #4390824, IDs8583) were used to generate transient knockdowns in hiPSC-CMs. Cells were seeded at 50,000 cells per well in a 96-well plate coated with 5 μ g/mL fibronectin. Cells were transfected as per the manufacturer protocol using either TransIT-TKO Transfection Reagent (Mirus Bio #MIR2154) or RNAiMax (Thermo Fisher Scientific #13778075) in iCell maintenance media containing 25 μ M Q-VD-OPh (QVD). To increase knockdown efficiency, the transfection was repeated 48 and 96 hours later. Cells were left to recover for an additional 24 hours in fresh media containing 25 μ M QVD. Cells were lysed for Western blot or re-plated on glass-bottom 35 mm dishes and fixed for analysis by

immunofluorescence. Silencer Select Negative Control No. 1 (Thermo Fisher Scientific # 4390843) was used as a control.

Plasmids encoding mito-tdEos (Addgene #57644) or GCaMP5G (Addgene #31788) were transfected using ViaFect (Promega #E4981) as described in the manufacturer protocol. Cells were maintained until optimal transfection efficiency was reached before cells were imaged.

Immunofluorescence

For immunofluorescence, cells were fixed with 4% paraformaldehyde for 20 min and permeabilized in 1% Triton-X-100 for 10 min at room temperature. After blocking in 10% BSA, cells were treated with primary and secondary antibodies using standard methods. Cells were mounted in Vectashield (Vector Laboratories #H-1000) prior to imaging. Primary antibodies used include Alexa Fluor-488 Phalloidin (Thermo Fisher Scientific #A12379), mouse anti-mtCO2 (Abcam #ab110258), and mouse anti-Mitochondria (Abcam #ab92824). For Incucyte experiments, nuclei were visualized using NuLight Rapid Red Reagent (Essen Bioscience #4717). Alexa Fluor-488 (Thermo Fisher Scientific #A11008) and Alexa Fluor-568 (Thermo Fisher Scientific #A11011) were used as secondary antibodies. MitoTracker Red CMXRos (Thermo Fisher Scientific #M7512) added at 100 nM was used to visualize mitochondria in PLA experiments.

Membrane fractionation

Cells were lysed in 1X CHAPS (Sigma #C5070-5G) containing protease and phosphatase inhibitors for 20 mins on ice while vortexing, followed by centrifugation at 14,000 rpm for 20 mins. The supernatant was collected (cytosolic fraction) and the pellet was resuspended in the same volume of 1X CHAPS buffer containing protease and phosphatase inhibitors. Lysates were then prepared for gel electrophoresis and Western blot as described below.

Western blot

Gel samples were prepared by mixing cell lysates with LDS sample buffer (Life Technologies, #NP0007) and 2-Mercaptoethanol (BioRad #1610710) and boiled at 95°C for 5 minutes. Samples were resolved on 4-20% Mini-PROTEAN TGX precast gels (BioRad #4561096) and transferred onto PVDF membrane (BioRad #1620177). Antibodies used for Western blotting are as follows: DRP-1 (Cell Signaling Technologies #8570S), pDRP-1 S616 (Cell Signaling Technologies #4494), OPA1 (Cell Signaling Technologies #67589S), MCL-1 (Cell Signaling Technologies #94296S), TOM20 (Cell Signaling Technologies # 42406S), VDAC (Cell Signaling Technologies #4866T) and α -Tubulin (Sigma # 05-829).

Impedance assays

The Axion Biosystems analyzer was used to measure contractility and impedance in iPSC-CMs. Cells were plated on 48-well CytoView MEA plates and maintained for 10 days before treatment and recordings. Recordings were taken for 5 minutes approximately two hours after media change at 37°C and 5% CO₂. Cells were assayed using the standard cardiac analog mode setting with 12.5 kHz sampling frequency to measure spontaneous cardiac beating. The Axion instrument was controlled using Maestro Pro firmware version 1.5.3.4. Cardiac beat detector settings are as follows:

Beat Detection Threshold	300 μ V
Min. Beat Period	250 ms
Max. Beat Period	5 s
Synchronized Beat Maximum Propagation Delay	30 ms
Minimum Active Channels Ratio	50.00%
Running Average Beat Count	10

Recordings for the hormone-matured hiPSC-CMs in Figure 6 were obtained using a

CardioExcyte96 instrument (Nanion Technologies). Cell preparation, data acquisition, and data processing were completed as described previously (Chavali et al., 2019).

Calcium imaging

Cells were transfected with GCaMP5G probe in 96-well plates and protein expression was allowed to stabilize for 48 hours. Cells were maintained on the microscope stage incubator for 30 minutes prior to imaging on a Nikon Eclipse Ti inverted microscope equipped with a 10X .30 NA objective. For each biological replicate, three technical replicates of a 10-second time-lapse recording were collected for each well. Baseline recordings were taken 24 hours prior to treatment. Subsequent recordings were taken 2 hours post treatment. Calcium intake was quantified in Fiji. Briefly, background fluorescence was first measured for intensity correction. A kymograph was then created using the Multiple Kymograph tool in Fiji using a 25-pixel thick line drawn across the entire cell. Calcium intake was measured as the ratio of the mean intensity of the brightest frame to the mean intensity of the darkest frame in the kymograph.

Plate-reader assays (CaspaseGlo 3/7 and CellTiter-Blue)

Cells were plated onto 1% gelatin-coated white round-bottomed 96-well plates at 20,000 cells/well. At least two duplicate wells were used per condition. At the end of inhibitor treatments, media was aspirated from the wells and a 1:1 ratio of CaspaseGlo 3/7 reagent (Promega #8091) and fresh media was added. The plates were incubated at room temperature for 1 hr in the dark and analyzed in a Promega GloMax luminometer according to manufacturer instructions. For the cell viability assay in Figure 5C, hiPSC-CMs were plated onto 1% gelatin-coated black clear-bottomed 96-well plates at 20,000 cells/well. Three replicate wells were used per condition. Cells were pre-treated with indicated inhibitors for 24 hours, followed by addition of fresh media and inhibitors or H₂O₂ for an additional 24 hours. 10% Triton-X-100 was added to untreated wells as a blank for normalization. CellTiter-Blue reagent was added to wells (20 μ L) and plates were

incubated at 37°C and 5% CO₂ for 2 hrs. Plates were analyzed in a POLARstar Omega plate-reader (BMG LabTech) according to manufacturer instructions.

Seahorse Mito Stress Test

hiPSC-CMs were plated from thaw onto 1% gelatin-coated Seahorse XF96 V3 PS cell culture microplates 7 days before the assay at 20,000 cells per well. 24 hours prior to the assay, inhibitor treatments were added to triplicate wells in maintenance media. One hour prior to the assay, media was switched to XF DMEM media containing 1 mM pyruvate, 2 mM glutamine, and 10 mM glucose. Oxygen consumption rate (OCR) was measured sequentially after addition of 1.0 μM oligomycin, 0.5 μM FCCP, and 0.5 μM rotenone.

Proximity Ligation Assay (PLA)

Cells were plated onto fibronectin-coated 8-chamber MatTek glass slides (#CCS-8) at 10,000 cells/chamber. After treatments, cells were fixed in 4% PFA for 20 min and permeabilized in 1% Triton-100-X for 10 min at room temperature. Following fixation, the DuoLink proximity ligation assay (Sigma #DUO92014) was performed as per manufacturer protocol. The primary antibodies were incubated overnight at 4°C and are as follows: mouse anti-MCL-1 (Proteintech # 66026-1-Ig), rabbit anti-DRP-1 (Cell Signaling Technologies #8570S), rabbit anti-OPA1 (Cell Signaling Technologies #67589S), and control containing no primary antibody.

Photoconversion experiments

Mitochondrial network connectivity and fusion was assayed using photo-conversion of mitochondria tagged with mito-tdEos (Addgene #57644). Photo-conversion was performed on a Nikon Eclipse Ti inverted widefield microscope equipped with a 1.45 NA 100X Oil objective. Briefly, a stimulation region was closing down the field diaphragm and using the filter to shine 405 nm light for 6 seconds. Images for the converted (TxRed) and unconverted (FITC) were acquired

before and after stimulation. The TxRed image before stimulation was used to subtract background from the post-stimulation images, followed by thresholding and automated measurement in Fiji (Schindelin et al., 2012). The initial converted area immediately after stimulation was used as a measure of connectivity, while the spread of the converted signal after 20 minutes was used as a measure of fusion/motility. The initial converted area (TxRed channel) was normalized to the total unconverted area (FITC channel) to account for any initial variation in the total mitochondrial area.

Image acquisition

Super-resolution images for Figures 1 and 2 were acquired using a GE DeltaVision OMX microscope equipped with a 1.42 NA 60X Oil objective and a sCMOS camera. Super-resolution images for Figures 1, 2, 7, S2 and S6 were acquired using a Nikon SIM microscope equipped with a 1.49 NA 100x Oil objective and an Andor DU-897 EMCCD camera. Images for Figures 4, S3 and S6 were acquired on a Nikon Eclipse Ti inverted widefield microscope equipped with a 1.45 NA 100X Oil or 1.40 NA 60X Oil objective. Image processing and quantification was performed using Fiji. Measurement of cell number to assay cell death was performed on a Incucyte S3 live cell imaging system (Essen Bioscience) equipped with a 10X objective. Images for the PLA experiments were acquired on a Nikon Eclipse Ti-E spinning disk confocal microscope equipped with a 1.40 NA 60X Oil objective and an Andor DU-897 EMCCD camera.

Statistical Analysis

All experiments were performed with a minimum of 3 biological replicates. Statistical significance was determined by unpaired, two-tailed Student's t-test or by one- or two-way ANOVA as appropriate for each experiment. GraphPad Prism v8.1.2 was used for all statistical analysis and data visualization.

Error bars in all bar graphs represent standard error of the mean or standard deviation as described for each figure, while Tukey plots were represented with boxes (with median, Q1, Q3 percentiles), whiskers (minimum and maximum values within 1.5 times interquartile range) and solid circles (outliers). No outliers were removed from the analyses.

For MEA experiments, means from triplicate biological replicates (each with 2-3 technical replicate wells) for each measurement were plotted and significance was determined by two-way ANOVA. 20 hour data was excluded for two-way ANOVA in Figure 2B-C and E-F, since this time-point was not recorded for ABT-199; likewise, ABT-199 was excluded from analysis in Figure 2D.

For PLA experiments, images were quantified using Fiji. Briefly, background noise levels were subtracted, and number of puncta per ROI was normalized to mitochondrial area. ROIs in at least 5 cells per condition were quantified in three independent experiments.

Quantification of mitochondrial morphology was performed in NIS-Elements (Nikon); briefly, we segmented mitochondria in 3D and performed skeletonization of the resulting 3D mask. Skeleton major axis and sphericity measurements were exported into Excel, and the data was filtered and analyzed in MatLab. Quantification of actin organization was performed in a blinded fashion and percentages of each category are displayed. Cell viability measured using the Incucyte live cell imaging system was performed by automatic segmentation of nuclei in Fiji, followed by subtraction of dead cells as indicated by fragmented nuclei and rounded phenotype detected by phase contrast.

Key Resources Table

REAGENT or RESOURCE	SOURCE	IDENTIFIER
Antibodies		
Mouse anti-mitochondria [113-1]	Abcam	Cat#Ab92824 RRID:AB_10562769
Mouse anti-mtCO2	Abcam	Cat#Ab110258; RRID:AB_10887758
Alexa Fluor-488 Phalloidin	Thermo Fisher Scientific	Cat#A12379

Alexa Fluor-488	Thermo Fisher Scientific	Cat#A11008, RRID:AB_143165
Alexa Fluor-568	Thermo Fisher Scientific	Cat#A1101; RRID:AB_143157
Rabbit anti-pDRP-1 S616	Cell Signaling Technologies	Cat#3455S; RRID:AB_2085352
Rabbit anti-DRP-1	Cell Signaling Technologies	Cat#8570S; RRID:AB_10950498
Rabbit anti-pDRP-1 S616	Cell Signaling Technologies	Cat#4494; RRID:AB_11178659
Rabbit anti-OPA1	Cell Signaling Technologies	Cat#67589S; RRID:AB_2799728
Rabbit anti-MCL-1	Cell Signaling Technologies	Cat#94296S; RRID:AB_2722740
Rabbit anti-Tom20	Cell Signaling Technologies	Cat#42406S; RRID:AB_2687663
Rabbit anti-VDAC	Cell Signaling Technologies	Cat#4866T; RRID:AB_2272627
Mouse α -Tubulin	Millipore	Cat#05-829; RRID:AB_310035
Mouse anti-MCL-1	Proteintech	Cat#66026-1-Ig; RRID:AB_11041711
Chemicals, Peptides, and Recombinant Proteins		
Fibronectin	Corning	Cat#354008
CHIR 99012 GSK-3 α and GSK-3 β inhibitor	Selleck Chemicals	Cat#S1263
IWR-1 tankyrase inhibitor	Sigma	Cat#I0161
S63845 MCL-1 inhibitor derivative	Joseph Opferman, St. Jude's Children Hospital	N/A
Q-VD-OPh pan-caspase inhibitor	SM Biochemicals	Cat#SMPH001
ABT-199 BCL-2 inhibitor	Active Biochemicals	Cat#A-1231
TransIT-TKO Transfection Reagent	Mirus Bio	Cat#MIR2154
Lipofectamine RNAiMax Transfection Reagent	Thermo Fisher Scientific	Cat#13778075
Silencer Select Negative Control No. 1	Thermo Fisher Scientific	Cat#4390843
Viafect transfection reagent	Promega	Cat#E4981
AZD5991 MCL-1 inhibitor	ChemieTek	Cat#CT-A5991
AMG-176 MCL-1 inhibitor	ChemieTek	Cat#CT-AMG176
IM-54 necrosis inhibitor	Santa Cruz Biotechnology	Cat#SC222053A
Hydrogen peroxide solution	Sigma	Cat#H1009
Critical Commercial Assays		
DuoLink Proximity Ligation Assay	Sigma	Cat#DUO92014
Seahorse XF Cell Mito Stress Test Kit	Agilent	Cat#103015-100
Caspase-Glo 3/7 Assay	Promega	Cat#8091
CellTiter-Blue Cell Viability Assay	Promega	Cat#8081
Experimental Models: Cell Lines		
Human: iCell Cardiomyocytes ² , iPSC-derived cardiomyocytes	Cellular Dynamics International	Cat#CMC-100-012-000.5
Oligonucleotides		
siRNA targeting DRP-1	Thermo Fisher Scientific	Cat#AM51331 ID19561
siRNA targeting MCL-1	Thermo Fisher Scientific	Cat#4390824, IDs8583
Recombinant DNA		

Plasmid encoding mito-tdEos (tdEos-Mito-7)	Addgene Shtengel et al., 2009	Cat#57644; RRID:Addgene_57644
Plasmid encoding GCaMP (pCMV-GCaMP5G)	Addgene Akerboom et al., 2012	Cat#31788, RRID:Addgene_31788
Software and Algorithms		
Maestro Pro firmware version 1.5.3.4	Axion Biosystems	https://www.axionbiosystems.com/applications/cardiac-activity
Fiji	Schindelin et al., 2012	https://imagej.net/Fiji
GraphPad Prism v8.1.2	GraphPad	https://www.graphpad.com/scientific-software/prism/
NIS-Elements AR	Nikon	https://www.nikon.com/products/microscope-solutions/lineup/img_soft/nis-elements/
Other		
iCell Cardiomyocyte maintenance medium	Cellular Dynamics International	Cat#M1003
NuLight Rapid Red Reagent	Essen Bioscience	Cat#4717
MitoTracker Red CMXRos	Thermo Fisher Scientific	Cat#M7512
Incucyte S3 live cell imaging system	Essen Bioscience	Cat#4763
CytoView microelectrode array plate – 48 wells	Axion Biosystems	Cat#M768-IMEA-48B
CytoView MAESTRO Pro MEA system	Axion Biosystems	N/A
Promega GloMax luminometer	Promega	N/A
POLARstar Omega plate-reader	BMG LabTech	N/A
Seahorse XF calibrant	Agilent	Cat#100840-000
Seahorse XF96 V3 PS cell culture microplates	Agilent	Cat#101085-004
Seahorse XFe96 Extracellular flux assay kits	Agilent	Cat#102601-100
Seahorse XFe96 Analyzer	Agilent	N/A
Seahorse XF DMEM medium pH 7.4	Agilent	Cat#103575-100
Seahorse XF 1.0 M glucose solution	Agilent	Cat#103577-100
Seahorse XF 100mM pyruvate solution	Agilent	Cat#103578-100
Seahorse XF 200 mM glutamine solution	Agilent	Cat#103579-100

Supplemental Information References

Chavali, N.V., Kryshtal, D.O., Parikh, S.S., Wang, L., Glazer, A.M., Blackwell, D.J., Kroncke, B.M., Shoemaker, M.B., Knollmann, B.C., 2019. Patient-independent human induced pluripotent stem cell model: A new tool for rapid determination of genetic variant pathogenicity in long QT syndrome. *Heart Rhythm* 16, 1686–1695.
<https://doi.org/10.1016/j.hrthm.2019.04.031>

Parikh, S.S., Blackwell, D.J., Gomez-Hurtado, N., Frisk, M., Wang, L., Kim, K., Dahl, C.P., Fiane, A., Tønnessen, T., Kryshtal, D.O., Louch, W.E., Knollmann, B.C., 2017. Thyroid and Glucocorticoid Hormones Promote Functional T-Tubule Development in Human-Induced Pluripotent Stem Cell-Derived Cardiomyocytes. *Circ. Res.* 121, 1323–1330.
<https://doi.org/10.1161/CIRCRESAHA.117.311920>

- Schindelin, J., Arganda-Carreras, I., Frise, E., Kaynig, V., Longair, M., Pietzsch, T., Preibisch, S., Rueden, C., Saalfeld, S., Schmid, B., Tinevez, J.-Y., White, D.J., Hartenstein, V., Eliceiri, K., Tomancak, P., Cardona, A., 2012. Fiji: an open-source platform for biological-image analysis. *Nat. Methods* 9, 676–682. <https://doi.org/10.1038/nmeth.2019>
- Wang, L., Kim, K., Parikh, S., Cadar, A.G., Bersell, K.R., He, H., Pinto, J.R., Kryshtal, D.O., Knollmann, B.C., 2018. Hypertrophic cardiomyopathy-linked mutation in troponin T causes myofibrillar disarray and pro-arrhythmic action potential changes in human iPSC cardiomyocytes. *J. Mol. Cell. Cardiol.* 114, 320–327. <https://doi.org/10.1016/j.yjmcc.2017.12.002>